Estimating Nocturnal Opaque Ice Cloud Optical Depth from MODIS Multispectral Infrared Radiances Using a Neural Network Method

Patrick Minnis[1], Gang Hong[2], Szedung Sun-Mack[2],

William L. Smith, Jr.[1], Yan Chen[2], and Steven D. Miller[3]

[1]*NASA Langley Research Center, Hampton, Virginia*

[2]*Science Systems and Applications, Inc., Hampton, Virginia*

[3]*Cooperative Institute for Research in the Atmosphere, Ft. Collins, CO*

• Information about nocturnal opaque ice cloud optical depth available in multispectral infrared temperatures

• Neural network algorithm developed to retrieve ice cloud optical depth from nighttime imager data based on CloudSat radar profiles of ice water content and particle size

• Realistic total cloud optical depth can be estimated from the neural network opaque ice cloud optical depth using a parameterization of cloud water path

Submitted to
Journal of Geophysical Research

2015

Abstract

Retrieval of ice cloud properties using IR measurements has a distinct advantage over the visible and near-IR techniques by providing consistent monitoring regardless of solar illumination conditions. Historically, the IR bands at 3.7, 6.7, 11.0, and 12.0 μm have been used to infer ice cloud parameters by various methods, but the reliable retrieval of ice cloud optical depth τ is limited to non-opaque cirrus with $\tau < 8$. The Ice Cloud Optical Depth from Infrared using a Neural network (ICODIN) method is developed in this paper by training MODerate-resolution Imaging Spectroradiometer (MODIS) radiances at 3.7, 6.7, 11.0, and 12.0 μm against CloudSat-estimated τ during the nighttime using 2 months of matched global data from 2007. An independent dataset consisting of comparable 2008 data was used to validate the ICODIN. One 4-channel and three 3-channel versions of the ICODIN were tested. The training and validation results show that IR channels can be used to estimate ice cloud τ up to ~70 or so with correlations above 78% and 69% for all clouds and only opaque ice clouds, respectively. The corresponding RMS differences relative to CloudSat are ~100 and ~72%. The 3.7-μm channel appears to be most sensitive to optical depth changes but is constrained by poor precision at low temperatures. A method for estimating total optical depth is explored for estimation of cloud water path in the future. Factors affecting the uncertainties and potential improvements are discussed. The method can ultimately improve cloud property monitoring over the entire diurnal cycle.

1. Introduction

Clouds comprise a key component of weather and climate. They alter the flow of solar and infrared radiation through the atmosphere between the surface and space, they serve as the source of precipitation, and their disappearance or formation affects the local sensible and latent heat balance. Because cloud processes occur throughout the diurnal cycle, it is critical for weather and climate models to accurately account for clouds both day and night. Numerical models require observations to develop understanding of the processes and to validate the results (e.g., *Fridlind et al*. [2012]). Additionally, direct assimilation of cloud properties, such as cloud optical depth [*Norris and da Silva*, 2015] or water path (*Jones et al.*, 2013, 2015a; *Chen et al.*, 2015], in weather models can demonstrably improve forecasts of critical parameters. The optimal source of cloud parameters for these weather and climate applications is satellite imager data, which provide contiguous spatial coverage and in the case of geostationary satellites, relatively continuous temporal coverage. Remote sensing of cloud properties from imager data has developed dramatically since the beginning of the satellite era and today provides a wealth of information about clouds in near-real time from a variety of satellites (e.g., *Minnis et al.* [2008]). Yet, there remain significant limitations on what can be retrieved using current algorithms, thus restricting the utility of the satellite data for providing critical cloud property information for weather and climate applications.

A full suite of cloud parameters can be determined from a combination of solar and infared channels on modern research and operational satellite imagers (e.g., *King et al.* [2003], *Heidinger et al.* [2003], *Minnis et al.* [2011b]). These include cloud fraction, top height and temperature, visible (~0.65 μm) optical depth τ, and effectives, particle radius r_e, among other variables. The cloud water path (CWP) can be derived, with some assumption from the product

of τ and r_e. At night, using only a limited number of infrared channels, it is possible to retrieve the same suite of variables, except that values of τ or r_e cannot be directly determined unless $\tau <$ 5 or so (*Szejwach*, 1982; *Inoue*, 1985; *Liou et al.*, 1990; *Lin and Coakley*, 1993; *Ou et al.*, 1993; *Huang et al.*, 2004; *Yue and Liou*, 2009; *Minnis et al.*, 2011b]. Without the solar reflectance channels, the retrievals are limited to semi-transparent clouds only. The retrieval algorithms can decide if a cloud is opaque at infrared wavelengths (e.g., *Hong et al.* [2010a]), but they cannot determine whether the cloud optical depth is 8 or 100, for example, due to a lack . Thus, the use of those cloud properties and CWP for weather and climate applications is confined to the daytime, a restriction that could compromise the utility of the data. For example, a short-term forecast of convective storms based on assimilated satellite-retrieved values of CWP could be significantly degraded at night if there is no reasonable estimate of CWP in the locations of important convective clouds and the near-storm environment (e.g., *Jones et al.* [2015b]).

The launch of the Suomi National Polar-orbiting Partnership (SNPP) satellite with the Visible Infrared Imaging Radiometer Suite (VIIRS) has made it possible to retrieve opaque cloud optical depth using a Day/Night band (DNB) that measures reflected moonlight [*Walther et al.*, 2014]. This exciting advance in cloud remote sensing is tempered by the complex nature of sources contributing to the light received by the sensor, which includes auroras, city lights, and fires [*Hillger et al.*, 2013]--making the approach most useful over the global oceans at low to mid-latitudes. Additionally, the intensity of the moonlight, though predictable [*Miller et al.*, 2009], is highly variable and is near zero for roughly half of the lunar cycle as viewed from the SNPP orbit. Thus, despite its great potential, the DNB channel cannot be used to continuously monitor the optical properties of optically thick clouds at night. A different approach is needed to provide a more comprehensive solution.

100 *Minnis et al.* [2012] demonstrated that brightness temperatures (BT) and brightness
101 temperature differences (BTD) at certain infrared wavelengths are sensitive to variations in τ and
102 r_e for values of τ up to 20 and possibly even to higher values of ~100. These wavelengths, 3.7,
103 6.7, 8.5, 10.8, and 12.0 μm, are similar to those among the channels onboard most modern
104 satellite imagers such as the MODerate-resolution Imaging Spectroradiometer (MODIS). A hint
105 of the sensitivity and correlation of the data is evident in Figure 1, which shows the ice water
106 path (IWP) and BTD between the 6.7 and 11-μm channels determined from the eastern
107 Geostationary Operational Environmental Satellite (GOES) imager data over the southern Great
108 Plains during a daytime hour. The IWP was retrieved with the method of *Minnis et al.* [2011b].
109 There is clearly some relationship between the two parameters, but it does not appear to be a
110 singular function. *Minnis et al.* [2012] found a dependence of BTD(6.7-11) on τ for a deep
111 convective cloud case, but because the radiance sensitivities to τ are quite small, especially for τ
112 > 20, the relationship can easily be lost in the measurement noise and model uncertainties. Thus,
113 a direct approach based on modeling the radiance fields is impractical for retrieving nocturnal
114 opaque ice cloud properties.
115 One method that skirts the need for a physical retrieval is the neural network. *Kox et al.*
116 [2014] developed a neural network method to determine τ and cloud top height Z_t for non-
117 opaque ice clouds using seven infrared channels as input and τ from the Cloud-Aerosol Lidar
118 with Orthogonal Polarization (CALIOP) on the Cloud-Aerosol Lidar and Infrared Pathfinder
119 Satellite Observation (CALIPSO; see *Winker et al.* [2007]) satellite as output. That algorithm,
120 applicable only to ice clouds having $\tau < 2.5$, proved quite successful at reproducing the
121 CALIOP-based retrievals of τ and Z_t from passive infrared data. In earlier preliminary studies
122 using MODIS data for input and retrievals based on CALIOP and CloudSat [*Stephens et al.*,

123 2002] Cloud Profiling Radar (CPR; *Im et al.* [2005]) data for output, *Hong et al.* [2010b, 2012]
124 found that a neural network approach might provide a reasonable estimate of τ for opaque ice
125 clouds. This method, however, has not yet been fully documented and analyzed in detail.
126 Nevertheless, it is clear that the neural network technique could prove valuable in overcoming
127 the apparently inherent limitations of using infrared data for cloud retrievals.

128 To address the need for obtaining reliable cloud optical depth information at night, this paper
129 expands on the initial work of *Hong et al.* [2010b, 2012] and *Minnis et al.* [2010, 2011a] to
130 document and further develop the use of a neural network to estimate τ for opaque ice clouds
131 using multispectral infrared brightness temperatures and their differences. Here, the target output
132 values consist of ice cloud optical depths from CPR data. They are available both day and night
133 and therefore serve as optimal reference sets for training the neural network. Multispectral
134 infrared data from MODIS are used as input data to train the neural network to estimate τ.
135 Because the channel complement differs from imager to imager, the technique, referred to as the
136 Ice Cloud Optical Depth from Infrared using a Neural network (ICODIN), is tested using
137 different combinations of channels centered near 3.7, 6.7, 10.8, and 12.0 μm. The method is
138 assessed using independent CPR data as well as daytime retrievals using the MODIS visible
139 channel and nighttime retrievals using the DNB from VIIRS. The potential uses and pitfalls of
140 the ICODIN are then discussed.

141 **2. Data**
142
143 The ICODIN is developed to complement nocturnal retrievals that retrieve cloud properties
144 for non-opaque clouds. The input data consist of multispectral radiances from passive imaging
145 radiomaeters that are assumed to be associated with optically thick, .e., opaque, ice clouds. The
146 output data are optical depths derived from the active sensor.

147 **2.1. Passive Satellite Data**

148 Nocturnal brightness temperatures from 1-km Aqua MODIS channels 20 (3.7 μm), 27 (6.7
149 μm), 31 (11.0 μm), and 32 (12.0 μm) from March and October of 2007 and 2008 are used as the
150 input for the ICODIN. The brightness temperatures are included among the results of an
151 intermediate step in the processing of the A-train CALIPSO, CloudSat, CERES, and MODIS
152 merged product (C3M, see *Kato et al.* [2010, 2011]). CERES is the Clouds and Earth's Radiant
153 Energy System [*Wielicki et al.* 1998] project. The C3M processing matches up to three
154 CALIPSO footprints with each MODIS pixel along its ground track. It then assigns the nearest
155 CloudSat footprint to each of those MODIS pixels. The cloud properties from MODIS, retrieved
156 using the algorithms of *Minnis et al.* [2011b], are included with the matched CALIPSO and
157 CloudSat products along with radiances from 18 MODIS channels. Those matched data,
158 constituting part of the C3M intermediate product, are used here. The CloudSat ground track is
159 parallel to Aqua and is viewed by MODIS at viewing zenith angles (VZA) up to 18°. No
160 corrections are made for parallax effects because of the small differences in VZA. Night is
161 defined here as the solar elevation being at least 3° below the horizon, that is, at solar zenith
162 angles exceeding 93°.

163 One Aqua MODIS image granule from July 2012 is used for comparison with matched SNPP
164 VIIRS DNB retrievals. Another Aqua MODIS granule from 2007 used for a daytime comparison
165 with the ICODIN output.

166 The standard CERES method for retrieving cloud properties at night is the Shortwave-
167 infrared Infrared Split window Technique (SIST; *Minnis et al.* [2011b]). The SIST uses BT(3.7),
168 BT(11), and BT(12) to retrieve T_c, τ, and r_e, where T_c is the effective radiating temperature of the
169 cloud (typically corresponding to an optical depth of ~1 below the geometric cloud top for

optically thick clouds). The SIST attempts retrievals up to $\tau > 16$ or even greater, in some cases, but often, it classifies the cloud as opaque and assigns default values of 8, 16, or 32 to clouds deemed as such. The SIST results exemplify the state of the art for estimating τ at night.

Because MODIS includes an 8.5-μm channel, a different method that leverages the 8.5-μm radiance is used to classify a pixel as opaque ice for purposes of developing the initial version of the ICODIN. In particular, a procedure that combines the bispectral technique of *Baum et al.* [2000] and the trispectral technique of *Choi et al.* [2007] is used to identify ice clouds. The bispectral technique determines ice phase by satisfying either of two tests: BT(8.5) ≤ 238 K or BTD(8.5–11) ≥ 0.5 K [*Baum et al.* 2000; *Menzel et al.* 2006], while the trispectral technique determines ice phase by satisfying one of three tests: BT(11) ≤ 238 K, BTD(11-12) ≥ 4.5 K, or BT(6.7) ≤ 234 K. Once classified as an ice cloud, the technique of *Hong et al.* [2010a] is used to classify the cloud as being opaque ($\tau \geq 8$) or semitransparent. These three methods are collectively denoted here as the Baum/Choi/Hong (BCH) technique.

Even though the SIST or the BCH determines a pixel's cloud as being opaque ice, CloudSat could have a different classification. The CPR-based τ estimate could be less than 8 and/or the phase could be entirely liquid for the pixel. In a comparison with the CALIOP phase classification for single-layered clouds, it was found that the SIST agreed with CALIPSO 94% of the time over snow and ice-free areas and 88% of the time over snow and ice-covered areas [*NASA*, 2015]. Compared with CloudSat and CALIPSO data, the BCH correctly identifies ~81% of the sampled upper tropospheric clouds as either opaque or semitransparent (*Hong et al.* [2010a]). While a portion of the misclassified pixels here are likely to be optically thin clouds, the phase of some opaque clouds will be misclassified in the supercooled temperature range. For those BCH retrievals classified as opaque ice, which are actually thin ice according to the CPR

retrieval, the unconstrained training output may force the revised retrieval to yield a non-opaque value of τ. The misidentification of a liquid water cloud as ice will also result in some errors in the results.

2.2. Active Satellite Data

A large sample of data representative of the input and output parameters in the retrieval process is needed to train the neural network method. The primary output parameter here is ice cloud optical depth. Neither CALIPSO nor CloudSat alone is sufficient for providing a complete picture of opaque cloud vertical structure. The CPR tends to miss thin clouds composed of small cloud particles (the minimum detection is −30 dBZ [*Stephens et al.*, 2008]) particularly those at the tops of opaque ice clouds. The CALIOP signal detects the ice crystals at cloud top missed by the CPR, but is completely attenuated by optically thick clouds ($\tau > 3$) [*Kato et al.*, 2010]. Therefore, the combination of CloudSat and CALIPSO data would provide the most complete cloud vertical profile. However, since the CALIOP typically measures an additional optical depth of only ~0.3 or less above the tops of opaque ice clouds determined from the CPR (e.g., *McGill et al.* [2004]) and the minimum τ of 8 is the target here, then the exclusion of the extra τ from CALIOP adds a potential underestimate of the total ice τ value of 1-12% depending on the total depth of the cloud. However, much larger relative biases could occur for clouds with $\tau < 8$. In those instances, CloudSat could underestimate the optical depth by 50% for $\tau = 2$. Nevertheless, given potential biases of up to 25% in the CloudSat retrievals [*Austin et al*. 2009], the absence of the CALIOP contribution to the total ice optical depth should have minimal impact on the estimates of truly opaque ice cloud τ values. Thus, the C3M CloudSat products are used alone to compute τ. The profiles of IWC and r_e in C3M are from the CloudSat L1B Release 4 2B-CWC-RO product [*Austin et al*. 2009], which includes three types of profiles. This study

uses the profile type which assumes that all hydrometeors above the altitude corresponding to -20°C are ice phase and below the level corresponding to 0°C are liquid. Between the 0° and -20°C levels, the proportion of ice increases linearly from 0 to 100% with decreasing temperature.

To obtain the optical thickness of opaque ice clouds, the vertical profiles of ice water content (IWC) that are derived from CloudSat are used to estimate the total optical thickness of ice clouds using

$$\tau = \sum \frac{3}{4} \frac{IWC}{r_e \rho} Q_e \Delta z, \quad (1)$$

where IWC and r_e are from CloudSat, ρ is ice particle density (0.917 g cm^{-3}), Δz is the vertical thickness of the ice cloud, and Q_e, the extinction coefficient for ice clouds, is given a value of 2 in this study.

The C3M global matched MODIS and CloudSat data from March and October 2007 are used as the training set. The March and October 2008 global matched data comprise the independent validation dataset.

3. Methodology

3.1. Neural Network Retrievals

Different from the direct retrieval of a parameter value using a representative physical model, neural network algorithms aim to identify the relationship between input and output variables by learning from a set of observed or simulated data [*Karayiannis and Venetsanopoulos*, 1993]. A neural network is a computer model composed of individual processing elements that are called neurons. The network can comprise multiple layers of neurons interconnected with other neurons in different layers that are referred to as the input, hidden, and output layers. The inputs are

processed by a weighted summation function to produce a sum that is passed to a transfer function. The weights are used to determine the level of influence a given input has on the output layer. The output of the transfer function is the output of the neurons. A neural network constructs a nonlinear numerical model of a physical process in terms of network parameters that are trained with input and output parameters to determine the weights for any given connection.

Figure 2 shows the architectural graph of a three-layer perceptron with an input layer, a hidden layer, and an output layer. The neurons of the input layer are represented by vector $\boldsymbol{P}(p_1, p_2,\ldots p_{m-1}, p_m)$, where m is the number of the input neurons or parameters. In the current study, m=10 is used for the neural network training. The 10 neurons of $\boldsymbol{P}$ are BT(3.7), BT(6.7), BT(11), and BT(12), BTD(3.7-6.7), BTD(3.7-11), BTD(6.7-11), BTD(11-12), latitude, and longitude. The number of neurons in the hidden layer is determined during neural network architecture design and adjusted to produce best neural network performance. Here, n=50 neurons are used in the hidden layer for training. The number of neurons in the output layer is the number of output parameters in the retrieval. In this case, the opaque ice cloud optical thickness τ, as indicated in Figure 1, is the lone output. The hidden layer weighting vector, $\boldsymbol{W}$, is given in the form of

$$\begin{pmatrix} w_{1,1} & w_{1,2} & \cdots & w_{1,n-1} & w_{1,n} \\ w_{2,1} & w_{2,2} & \cdots & w_{2,n-1} & w_{2,n} \\ \vdots & \vdots & \ddots & \vdots & \vdots \\ w_{m-1,1} & w_{m-1,2} & \cdots & w_{m-1,n-1} & w_{m-1,n} \\ w_{m,1} & w_{m,2} & \cdots & w_{m,n-1} & w_{m,n} \end{pmatrix}, \quad (255)$$

where $w_{m,n}$ is the weight between input neuron, p_m, and hidden neuron, n. The output layer weighting vector, $\boldsymbol{V}(v_1, v_2, \ldots, v_{n-1}, v_n)$ comprises the weights between the hidden neurons and the output neuron. The vector, $\boldsymbol{B}(b_1, b_2, \ldots, b_{n-1}, b_n)$ is the bias in the hidden layer and b is the bias in the output layer.

260 The network training function of Bayesian regulation backpropagation is used for the three-
261 layer neural network. This training function updates the weight and bias values according to
262 Levenberg-Marquardt optimization. It minimizes a combination of squared errors and weights,
263 and then determines the correct combination so as to produce a network that generalizes well.
264 During the training, different transfer functions between the input and hidden layers and between
265 the hidden and output layers were investigated. It was found through initial testing that using a
266 log-sigmoid transfer function $s(x)$ to propagate to the hidden layer and a hyperbolic tangent
267 sigmoid transfer function $t(x)$ to propagate to the output layer produces the optimal network
268 performance. The log-sigmoid and the hyperbolic tangent sigmoid transfer functions,
269 respectively, are

270 $$s(x) = \frac{1}{1+\exp(-x)}, \qquad (2)$$

271 and

272 $$t(x) = \frac{2}{1+\exp(-2x)} - 1. \qquad (3)$$

273 During initial trials using this approach, both r_e and τ were selected for output. However, no
274 skill was found for estimating r_e, so as noted above, the analysis seeks only one output
275 parameter, τ.

276 The training was performed for all MODIS pixels classified as opaque ice by the BCH
277 method and having BT(11) < 260 K, which is warmer than the center of the supercooled
278 temperature range but substantially colder than the freezing level. Temperatures colder than 260
279 K are often associated with thick ice clouds such as cirrus anvils or deep convective elements
280 (e.g., *Tian et al.* [2004]). Additionally, the training was performed separately for pixels having
281 BT(11) < 250, 240, and 235K, to determine if the skill could be improved by additional

282 classification. This approach implicitly assumes that no optically thick ice clouds occur with top
283 temperatures greater than 260 K.

284 The ICODIN was trained using 4 different combinations of channels: a 4-channel method
285 using BT(3.7), BT(6.7), BT(11), and BT(12) and relevant BTDs denoted as ICODIN4 and three
286 3-channel methods. The ICODIN3a, which uses BT(6.7), BT(11), BT(12), BTD(6.7-11), and
287 BTD(11-12) is applicable day and night, while ICODIN3b, which uses BT(3.7), BT(11), BT(12),
288 BTD(3.7-11), and BTD(11-12), can be used on sensors lacking a 6.7-μm channel. A third night-
289 only version, ICODIN3c uses BT(3.7), BT(6.7), BT(11), BTD(3.7-6.7), BTD(3.7-11), and
290 BTD(6.7-11) and could be used for sensors lacking a 12-μm channel.

291 During the training, out of the total about 1.6 million collocated data for 2007 meeting the
292 criteria listed earlier, one out of every three pixels was selected for the training process. Of those
293 selected pixels, 60% were selected randomly to comprise the training set, which was employed
294 to compute the gradient and update the network weights and biases. Of the remainder, 20% were
295 extracted for validation and 20% were used for testing. Computer memory limitations
296 necessitated this downsizing of the dataset. The independent 2008 dataset included ~1.7 million
297 pixels, which is roughly 34% of the total number of C3M pixels for the time period. After
298 training, the ICODIN method was applied to all of the 2007 and 2008 data.

299 **3.2 Passive retrievals**

300 In addition to the raw MODIS BT and BTD data used in the ICODIN, the SIST was also run
301 for comparison. The SIST classified ~1.1 million pixels as opaque ice ($\tau \geq 8$) having BT(11) <
302 260 K, or ~22% of all pixels. Of those SIST opaque ice pixels, the SIST and BCH shared 59%,
303 leaving 0.45 million pixels classified as opaque ice by SIST and not by BCH. Conversely, the
304 BCH classified 0.65 million pixels as opaque ice that were not similarly identified by the SIST.

305 Cloud properties were derived from one 2007 daytime MODIS granule using the Visible
306 Infrared Shortwave-infrared Split-window Technique (VISST; see *Minnis et al.* [2011b]). The
307 SIST was used for selected granules to evaluate the performance of the ICODIN at night.
308 A nighttime SNPP VIIRS image granule was also analyzed using the VISST, but with the
309 DNB substituting for the visible (0.65 μm) channel. It was assumed that the cloud reflectance at
310 0.65 μm is the same for the DNB bandwidth so that the daytime reflectance model used by the
311 VISST [*Yang et al.* 2008] could be used at night. The DNB channel is much broader (0.5 – 0.9
312 μm) than the MODIS visible channel (0.615-0.678) so that some error will occur based on this
313 assumption. The incoming moonlight intensity was computed using a model described by *Miller*
314 *at al.* [2009]. Using those algorithms for this particular case yielded optical depths exceeding 135
315 for most of the convective clouds. As this is unlikely, based on daytime observations, the DNB
316 calibration gain was adjusted such that the brightest pixel yielded $\tau = 150$. The result of this
317 adjustment was a distribution of optical depths comparable to those seen during daytime.

318 **4. Results**

319 Results are presented for all versions of the ICODIN.

320 **4.1 4-channel Neural Network (ICODIN4) Training and Validation**

321 To determine the optimal set of temperature thresholds for using ICODIN, histograms of τ
322 from CloudSat and the four ICODIN4 training and validation runs were created and plotted as
323 shown in Figure 3. CloudSat results are shown as bold lines, while the various ICODIN4 results
324 are shown as thin lines and the various temperature thresholds used are distinguished by color.
325 Frequencies for $\tau < 50$ are shown Figures 3a and 3b for BT(11) < 260 and 235 K and for BT(11)
326 < 250 and 240 K, respectively. Similarly, Figures 3c and 3d show the corresponding results for
327 optical depths between 30 and 150 on a different scale. The ICODIN and CloudSat distributions

328 in Figure 3 are close, but not identical. The greatest divergences appear for $\tau < 10$ for BT(11) <
329 260 and 250 K, for $\tau < 20$ for BT(11) < 240K, and between $\tau = 10$ and 20 for BT(11) < 235 K.
330 All of the curves drop off exponentially from $\tau < 2$. It is clear that many of "opaque" pixels as
331 determined by the imager retrievals contain ice clouds having $\tau < 8$. Overall, 68% of the clouds
332 identified as opaque ice by the BCH method were determined to be semitransparent ($\tau < 8$) by
333 CloudSat. Similar results (48%) were found for the SIST method. This apparent misidentification
334 by the BCH and SIST probably involves impacts of phase misclassification and optical depth
335 errors in the imager retrievals, uncertainties in the CloudSat retrieval and assumed phase, and the
336 occurrence of thin ice clouds over water clouds with only small or no vertical separation between
337 the layers. That last condition would likely result in a false determination of opaque ice by one or
338 both of the passive methods.

339 Here, it is assumed that an optimal approach is that which would produce the same
340 distributions of τ as observed by CloudSat. To determine the temperature threshold that yields
341 the optimal statistical representation of the CloudSat ice cloud optical depths τ_{CS}, the ratio,
342 $N(\tau_{CN4}) / N(\tau_{CS})$, was plotted (Figure 4) for both the 2007 and 2008 results, where τ_{CN4} is the
343 ICODIN4 optical depth and N is the number of samples in a given optical depth bin. The ratios
344 for $\tau < 50$ and $\tau \geq 50$ for 2007 are plotted in Figures 4a and 4b, respectively. Their 2008
345 counterparts are shown in Figures 4c and 4d. For both 2007 and 2008, the ratio is closest to 1.0
346 for BT(11) < 260 K for τ between 8 and 50. For $\tau < 8$, all thresholds produce large errors, except
347 for BT(11) < 235 K during 2007. For $\tau > 50$ (right panels), the ratio drops almost linearly from
348 near unity to near zero at $\tau = 150$, indicating much reduced skill for retrieving values of $\tau > 60$
349 using ICODIN4. The black curve is mostly on top for 2007 (Figure 4b), while the red curve
350 appears to yield more for $\tau > 120$ or so for 2008 (Figure 4d). Considering the complexity in

application and the evident uncertainties for each threshold, it was decided to use the training set for BT(11) < 260 K, except when the set for BT(11) < 235 K produces a value of $\tau > 110$. The latter set is used to maximize the retrieval of the larger optical depths. Although the ratios were near unity for BT(11) < 235 K and $\tau_{CS} < 8$, including that criterion in the method made no difference in the overall agreement with τ_{CS}. Thus, the combination of the two training sets noted above constitutes the method used hereafter for all forms of the ICODIN.

The final training results using the four channels are shown as a density scatterplot in Figure 5a, where the bin size is one optical depth unit. Additionally, the results of applying the trained neural network to the 2008 collocated C3M data are shown in Figure 5b. They constitute an independent validation, providing a measure of the robustness of the neural network approach. The goal of this study is to estimate τ for opaque ice clouds. It is clear in Figure 5 that semitransparent clouds are more common in this dataset despite the best efforts of the BCH to identify opaque clouds. Nevertheless, the ICODIN tends to reclassify thos "thin" opaque clouds. Both the 2007 training and independent 2008 results have correlation coefficients, *R*, exceeding 0.77 between the τ_{CN4} and τ_{CS} values. The bias for the training results is only -0.8%, while the 2008 bias is -1.2%. The corresponding standard deviations of the differences (SDD) are 99 and 105%. The accuracy of the ICODIN4 applied to an independent dataset is only slightly degraded and, therefore, should be generally applicable to all MODIS data, at least, for those observations near nadir.

The sample densities of scatterplots in Figure 5 do not coincide with the line of agreement. As expected from the results in Figure 4, the ICODIN4 results at the low end ($\tau < 15$) are mostly greater than the CPR values, while the opposite occurs at the high end. There, relatively few ICODIN4 values exceed 70, however, there are τ_{CN4} values as large as 100, but fewer than 5 (not

374 shown) in a given optical depth pair. Thus, the ICODIN4 tends to dampen the range, but still
375 yields a relatively high correlation. To determine if the results are imbalanced, the mean values
376 of τ_{CN4} and τ_{CS} were computed for every 2.5 ICODIN4 optical depth intervals between 0 and 50
377 and for every 5 optical depth intervals for $\tau_{CN4} > 50$. Figure 6 shows the binned averages
378 connected by a line. The means tend to follow the line of agreement up to $\tau_{CN4} \sim 70$ and then
379 diverge with the 2007 and 2008 data going above and below the line, respectively. The
380 divergence suggests that either the sample set is too small for the larger optical depths or the
381 information content is diminished, or both. Given the trends in Figures 4b and 4d, it is likely that
382 the information content is greatly diminished as τ increases beyond 50. However, these results
383 show that, on average, for any given value of $\tau_{CS} < 70$, τ_{CN4} is unbiased relative to τ_{CS}.
384 The damping effect of the neural network on the extreme values, suggested by Figure 4, can
385 also be seen in regional averages. Figure 7 plots the average nighttime opaque ice cloud optical
386 depth for 2° latitude by 2° longitude regions from the CPR and from MODIS using ICODIN4.
387 While the patterns are very similar, the CloudSat retrievals have more dark blue ($\tau < 5$) areas,
388 especially in higher latitudes and more red ($\tau > 50$) regions, particularly in the tropics. The
389 ICODIN4 means tend to be smoother than their CPR counterparts. The regional averages are
390 compared in a scatterplot (Figure 8), which shows that, overall, the means are unbiased and the
391 mean regional difference could be as large as 65% at the one standard deviation level. It is clear
392 from the plot that for many regions, the ICODIN4 overestimates the mean τ by 1-2 for $\tau < 3$ and
393 underestimates the mean for $\tau > 15$ or so.
394 Figure 9 shows an example of the ICODIN4 applied to MODIS data along the CloudSat
395 ground track for a MODIS granule taken over the tropical eastern Pacific at 0830 UTC 25 July
396 2008. The track, shown as a line over the multispectral (Figure 9a) and BT(11) (Figure 9b)

397 images, passes through areas of deep convection separated by low clouds. The line is black
398 except over opaque ice clouds where it is red. The CPR reflectivity image for the ground track
399 segment between 8°N and 14°N (Figure 9c) shows cloud tops reaching 15 km and a melting
400 layer near 5 km with two deep cells around 10°N. The corresponding optical depths retrieved
401 from the CPR and MODIS are plotted as blue and red points, respectively, in Figure 9d. Values
402 of τ_{CN4} and τ_{CS} track well for much of the segment, but τ_{CN4} tends to deviate at the extremes,
403 underestimating the highest values and overestimating many of the lower values, as discussed
404 above. Nevertheless, the results are quite encouraging and provide more relevant information
405 about opaque ice clouds than any default values.

406 This can be seen clearly in Figure 10, which compares the results of the ICODIN4 and the
407 SIST applied to the entire MODIS granule in Figure 9. Despite the lack of training at off-nadir
408 VZAs, the ICODIN4 (Figure 10a) produces a very reasonable distribution of τ values compared
409 to the images in Figure 9a, b. Few, if any pixels in the northwestern sector have $\tau_{CN4} > 100$,
410 while a large area of $\tau_{CN4} > 100$ is evident for the massive convective system near 6°N, 87°W,
411 which is dominated by pixels having BT(11) < 200 K. These distributions can be contrasted with
412 the SIST results (Figure 10c) from the CERES Edition 4 analyses [*Minnis et al.* 2010] that have
413 values of 32 for most of the colder clouds. If the SIST is used to select the opaque clouds (Figure
414 10b), fewer areas are selected as opaque clouds but some different areas (e.g., near 4°N, 92°W)
415 are classified as opaque by the SIST. Most of the clouds that appear to be optically thick visually
416 are selected by both methods.

417 **4.2. 3-channel Neural Network (ICODIN3a, b, c) Training and Validation**

418 The ICODIN3a (no 3.7-μm channel), the ICODIN3b (no 6.7-μm channel), and ICODIN3c
419 (no 12-μm channel) were trained and validated using the same datasets employed for ICODIN4.

420 The resulting statistics are shown in Table 1 along with those from the ICODIN4 analysis. A
421 total of 537,320 and 1,732, 361 matched points were used in ICODIN4 for 2007 and 2008,
422 respectively. The greater number of points in 2008 was possible because the training (2007) was
423 limited by computer memory and the application of the trained algorithm (2008) is not
424 constrained to keep all data in memory. Slightly different numbers of pixels were identified as
425 valid for the ICODIN3 analyses, thus different mean optical depth values were obtained for each
426 case. Overall, ICODIN4 produces the best statistical comparison with τ_{CS}, but the results from
427 the various 3-channel methods are not greatly different from the ICODIN4 statistics. The worst
428 performer is ICODIN3a, which lacks the 3.7-μm channel. Its correlation is lowest for the
429 independent retrievals and the SDD values are greatest overall. Increases in uncertainty occur
430 across the board for the 2008 data.

431 Figure 11 shows the optical depths retrieved using the ICODIN3a, ICODIN3b, and
432 ICODIN3c for the image analyzed in Figure 10. All three methods produce τ patterns similar to
433 those generated by ICODIN4 (Figure 10a), but each finds more extremely high (red) values for
434 the large system on the right than ICODIN4. ICODIN3a (Figure 11b) yields more low values
435 (black) of τ_{CN3a} on the center right and fewer values around 35 or so (dark blue). The ICODIN3b
436 (Figure 11c) more closely resembles the ICODIN4 results overall, but tends to run high.
437 ICODIN3c (Figure 11d) is also more like ICODIN4 than ICODIN3b, but has fewer extremely
438 high values overall.

439 The differences and similarities between the 3- and 4-channel methods are quantified in
440 Figure 12, which shows scatterplots made from the data in Figures 10a and 11. Optical depths
441 from ICODIN3a and ICODIN4 (Figure 12a) are highly correlated (R = 0.91), but the scatter is
442 quite high with SDD = 9.55, a value larger than that between τ_{CS} and τ_{CN4} (Table 1). The absence

443 of the water vapor channel in ICODIN3b does not seem to make a great amount of difference
444 compared to ICODIN4 as R = 0.97 and SDD = 5.53 (Figure 12b). Furthermore, the values at the
445 high end are mostly greater than those from ICODIN4, a tendency that may counteract the
446 shortfall in extremely high values seen in Figure 4. Unlike the nearly linear distribution of points
447 in Figure 12b, the results of ICODN3c (Figure 12c) yield a clearly non-linear relationship with
448 an inflection around $\tau_{CN4} \sim 70$ and an overestimating bulge around $\tau_{CS} \sim 25$. Its SDD value is
449 10% greater than its ICODIN3b counterpart. Although the results in Table 1 all give comparable
450 optical depths relative to CloudSat, Figure 12 indicates that the absence of the 6.7-μm channel
451 has the least impact on results. Or, since these data are from the entire image with VZAs up to
452 67°, they could indicate that the 6.7-μm (3.7-μm) channel is most (least) sensitive to VZA
453 effects.
454
455 **5. Discussion**
456 The ICODIN approach has skill at retrieving the ice cloud optical depth, but appears to have
457 relatively large random uncertainties. Moreover, it only retrieves the ice cloud optical depth and
458 makes no attempt to retrieve the total optical depth, which would include any liquid water in the
459 column. The uncertainties and the impact of ignoring the liquid water are discussed below. It is
460 beyond the scope of this paper to provide a complete error analysis. Rather, the purpose is to
461 demonstrate the potential of the ICODIN approach and illuminate some of the factors that should
462 be considered when further developing and applying it.
463 **5.1 Uncertainties**
464 As seen in the analysis above, the retrieved ice optical depths are relatively unbiased, on
465 average, but the RMS errors (~SDD) are on the order of 100%. These errors are likely due to

466 limitations in the ICODIN retrievals and to uncertainties in the CloudSat retrievals. As discussed
467 in *Minnis et al.* [2012], the sensitivity of the ICODIN channels to changes in optical depth
468 beyond the infrared opaque "limit" is likely due to subtle changes in the cloud top structure and,
469 especially for 6.7 μm, the water vapor in the top levels of the cloud. The relationships among the
470 vertical structure, the ice optical depth, and the individual channel responses are probably not
471 unique, which would account for some of the scatter and the decreasing ability to detect a
472 dependence on τ at values greater than ~60. For example, the vertical structure at cloud top could
473 be the same for a cloud having τ = 70 or 100 in some cases, but not in others. Because the
474 development of very thick ice clouds is mostly a deep convective phenomenon, τ is also likely to
475 be affected by the vertical profiles of temperature and humidity, the surface temperature, and the
476 stability. In this study, those factors, as well as surface type, were not considered.
477 At the bottom of the temperature range (BT < 220 K), values of BT(3.7) change by several K
478 / count, drastically reducing the precision of the observation. For extremely cold clouds having
479 very large optical depths, the 3.7-μm channel yields very noisy (and hence, uncertain)
480 temperatures that can be either larger or smaller than their 11-μm counterparts. This is illustrated
481 in Figure 13, which shows BT(11) and BTD(3.7-11) for a MODIS image of a convective system
482 over the northeast Pacific at 0925 UTC, 5 July 2012. The BTD (Figure 13b) peaks above 30 K
483 for BT(11) ~ 245 K (Figure 13a). It drops with decreasing BT(11) to 3 or 4 K near 220 K and
484 then varies between -5 and +10 K for BT(11) < 220K. Striping is evident for the coldest
485 temperatures. Inaccurate temperatures would reduce the potential for providing a distinct optical
486 depth signal that could be exploited by the ICODIN. The apparent capability of retrieving more
487 large optical depths without the 6.7-μm channel (Figure 12b), however, suggests that this is not
488 an issue. On the other hand, the 3-channel combination lacking the 3.7-μm data (Figure 12c) has

489 the fewest values of $\tau > 100$. This suggests that the 3.7-μm channel is most sensitive to τ, so that
490 having smaller errors in BT(3.7) at the low end of the range (180-200 K) could lead to the
491 retrieval of more values of $\tau > 70$. This is consistent with the detailed radiative transfer
492 calculations in *Minnis et al.* [2012] that show BTDs using BT(3.7) continue to decrease toward
493 zero for $\tau > 100$.

494 Because the thermal radiation channels used here are sensitive to the vertical profiles of IWC
495 and particle size, the measured radiances that serve as input to the ICODIN can be affected by
496 subtle variations in the vertical profiles of those parameters, especially near cloud top. The
497 CloudSat retrievals used to train the ICODIN, however, are based on retrievals of IWC that can
498 be highly uncertain. In addition to being biased high by ~25% relative to in situ measurements,
499 the uncertainty in the individual retrievals often exceeds 100% (*Austin et al.* [2009]), especially
500 for lower temperatures, IWC < 0.1 gm^{-3}, and for clouds having $\tau < 15$. Thus, some of the
501 sensitivity to variations in IWC that can affect the passive radiances is not likely being faithfully
502 represented in the training set's output data. Thus, uncertainties of 100% in the ICODIN
503 retrievals are not surprising.

504 The goal of developing the neural network method here was to retrieve optical depths for
505 opaque clouds as defined by the BCH. Yet, a large fraction of the ice clouds identified as opaque
506 by the BCH or the SIST were classified as semitransparent by the CloudSat analysis. Those
507 retrievals are included in the statistics in Table 1. Computing the difference statistics only for
508 clouds classified as opaque by the ICODIN or by CloudSat provides a better representation of
509 how well the original goal was met. Tables 2 and 3 list the difference statistics for those MODIS
510 pixels having $\tau_{CS} \geq 8$ and $\tau_{CN} \geq 8$, respectively. Removing the smaller CloudSat optical depths
511 (Table 2) yields lower correlations and a significant bias in the ICODIN results, as expected from

512 Figures 4 and 5. The -20% bias in the mean τ_{CN} for $\tau_{CS} \geq 8$ is accompanied by a ~20% decrease
513 in SDD indicating that many of the largest relative uncertainties in Table 1 were due to clouds
514 having lower optical depths. In Table 3, the correlations are similar to those in Table 2, but the
515 biases are eliminated and the SDDs drop by another few percent. Thus, when the ICODIN (not
516 the BCH) classifies the cloud as opaque, it will, on average, have the same ice cloud optical
517 depth as the CloudSat retrieval.

518 The original goal, then, is partially met. Of the total number of pixels originally identified as
519 opaque, ~67% are semitransparent and ~33% are opaque, according to ICODIN4. The pixels
520 having $\tau_{CN} < 8$ and $\tau_{CS} \geq 8$ comprise ~7% of the total fraction of pixels. This identification
521 agreement or lack thereof is summarized in Table 4, which breaks down the various
522 classifications for the ICODIN4 and CloudSat results by percent of the total number of pixels.
523 Both ICODIN4 and CloudSat agree on the classification ~84% of the time. The disagreement is
524 nearly balanced with ICODIN4, on the whole, producing 1-2% more opaque clouds than
525 CloudSat. The near balance is also seen in the optical depths. For those pixels having $\tau_{CN} < 8$ and
526 $\tau_{CS} \geq 8$, the average $\tau_{CN} = 4.7$, while the mean τ_{CN} is 12.5 for those having $\tau_{CN} \geq 8$ and $\tau_{CS} < 8$.
527 The misclassification of ~68% of the pixels as opaque by BCH suggests the need to develop a
528 more accurate opaque ice cloud screening technique. However, the correct (according to
529 CloudSat) reclassification of ~60% of the BCH opaque pixels as semitransparent indicates that
530 ICODIN4 can also serve as an effective screening method for many semitransparent ice clouds.

531 **5.2 Comparisons with other retrievals**

532 Currently, thick cloud optical depths are mostly retrieved using reflected solar radiation
533 measurements. However, such retrievals yield the total cloud optical depth and not the separate
534 contributions from ice and water hydrometeors that together often comprise the observed cloud.

535 Optically thick ice clouds are commonly part of convective systems that are vertically
536 contiguous with liquid water clouds or that have anvils overlying low clouds, or that are part of a
537 baroclinic system with layers of liquid clouds below the ice layers. Despite these potential
538 differences, it is necessary to compare the ICODIN retrievals with their reflectance-based
539 counterparts to determine how they are related since the goal is to eventually develop a total
540 visible optical depth τ_V at night that matches the daytime retrievals as closely as possible. To
541 begin that process, two comparisons are made here.

542 Figure 14 shows the results for a nocturnal case from an Aqua MODIS image over the
543 tropical eastern Pacific at 0925 UTC, 5 July 2012. The pseudo-RGB image (Figure 14a) reveals
544 areas of deep convection in various stages of development and dissipation. This case was
545 selected because the Aqua and SNPP overpasses match closely so that VIIRS and MODIS view
546 essentially the same area at the same time. The optical depths from MODIS using ICODIN4 are
547 shown in Figures 14b and 14c using the BCH and SIST, respectively, to select thick ice clouds.
548 The results based on SIST are the same as those using the BCH criteria except that the SIST
549 appears to identify some thin cirrus over low clouds as being opaque (~5.5°N, 116°W). If the
550 SIST alone is used to determine the optical depths (Figure 14d), much of the selected cloud area
551 is set to the default value of 32. These results can be compared with the DNB retrievals from
552 VIIRS in Figure 14e, which shows many clouds having $\tau_{DNB} > 120$. In most instances, $\tau_{DNB} >$
553 τ_{CN4}. As noted above, this result is not surprising given that a significant portion of the cloud
554 column is likely in liquid form and ICODIN typically underestimates the ice cloud optical depth
555 when it exceeds 70. This can be seen in the light blue areas in Figure 14b/c, which have values of
556 60-70, while the DNB optical depths are mostly red with $\tau_{DNB} > 120$.

557 Similarly, Figure 15 gives an example of applying ICODIN3a to a daytime image, in this
558 case, from Aqua MODIS data taken over the tropical western Pacific at 0235 UTC, 1 February
559 2007. The pseudo-RGB and BT(11) images in Figures 15a and b, respectively, indicate areas of
560 very deep convection (dark blue in Figure 15b) with low clouds scattered among the ice cloud
561 areas. The ICODIN3a retrievals were performed using the BCH (Figure 15c) and VISST (Figure
562 15d) criteria for optically thick ice clouds. During daytime, the VISST retrieves optical depth
563 directly from the 0.65-μm reflectance, so the opacity should be less uncertain than when using
564 SIST. The ICODIN3a retrievals can be compared to the VISST optical depths in Figure 15e. As
565 in the DNB case, the optical depths from the neural network approach are generally less than
566 their VISST counterparts, however, there appear to be more instances where the $\tau_{CN3a} > \tau_{VISST}$
567 than for the DNB case in Figure 14. This could be expected to happen based on the noisier
568 ICODIN3a retrievals shown in Figure 12, which have considerable scatter relative to their
569 ICODIN4 counterparts and should, therefore, over- or underestimate τ_{CS} by greater amounts than
570 ICODIN4.

571 Daytime retrievals of τ or IWP for thick ice clouds, similar to those in Figures 14 and 15,
572 generally assume that the cloud is entirely ice and the effective particle size for the entire cloud
573 is the same as the retrieved value, even though it often represents only the top portion of the
574 cloud column. As shown by *Minnis et al.* [2007] and others, the true total optical depth retrieved
575 with that assumption will typically be underestimated by τ_{VISST} or τ_{DNB}, but that is a problem
576 addressed elsewhere [*Smith et al.* 2015]. The parameter, τ_{VISST}, retrieved at solar wavelengths
577 uses the single-phase assumption. Thus, to achieve parity between τ_{CS} or τ_{CN} and τ_{VISST}, it is
578 necessary to find some means for estimating τ_V from the ice optical depth.

579 For purposes of demonstration, τ_V is estimated here for the two images in Figures 14b and
580 15c using one of potentially many approaches. *Smith* [2014] developed a method for estimating
581 vertical profiles of cloud water content (CWC) based on MODIS retrievals of T_c, τ_{VISST}, and
582 IWP_{VISST} matched to CloudSat CWC that also yielded a parameterization of the IWP_{CS} as a
583 function of IWP_{VISST}, which is typically underestimated for optically thick ice clouds because of
584 larger particle sizes in the interior of the cloud than at cloud top. *Smith et al.* [2015] applied the
585 parameterization, which assumes that liquid water comprises a portion of the ice cloud whenever
586 $\tau_{VISST} > 10$, to more than 250,000 GOES pixels and tabulated the resulting mean values of τ_{VISST}
587 and IWP_{CS} for six intervals of τ_{VISST}. Assuming equivalence of τ_{CS} and τ_{CN}, and that r_e of the ice
588 portion of the cloud increases with IWP_{CS} from 30 to 80 μm, the estimated value of τ_{CN} was
589 computed as the product, 1.5* IWP_{CS} / r_e. With those assumptions, the resulting relationship is
590
591 $$\tau_V = 0.976 * \tau_{CN} + 0.0115*\tau_{CN}^2. \quad (4)$$
592
593 Equation (4) was applied to values of $\tau_{CN} > 10$ from BCH-ICODIN for the images in Figures
594 14 and 15. The results are compared in Figure 16 to those from VISST applied during the night
595 using the VIIRS DNB channel (Figure 14e, 16a) and during the day using the MODIS visible
596 channel (Figure 15d, 16c). The nocturnal values of τ_V (Figure 16b) appear to be much closer to
597 their DNB counterparts (Figure 16a) than the τ_{CN4} results (Figure 14b). Except for the more
598 contiguous red areas in the main cloud mass (upper right), few areas of overestimation are
599 evident. However, τ_{DNB} for the brightest clouds in the other systems remains underestimated by
600 τ_V. This is likely due to the large optical depth limitations discussed earlier, although the DNB
601 retrievals could be biased. Nevertheless, this initial result is encouraging for providing a

602 reasonable total optical depth estimate for these thick ice clouds at night. With proper
603 assumptions about the effective radii of the ice and water portions of those clouds, a more
604 realistic estimate of CWP could also be made.

605 The potential for estimating τ_V during daytime with infrared data only is less encouraging,
606 but not out of the realm of possibility. It is clear in Figure 16d that τ_V both under- and
607 overestimates the corresponding τ_{VISST} retrievals (Figure 16c) much more frequently than in the
608 DNB case. While τ_V is considerably closer to τ_{VISST} than τ_{CN3a} (Figure 15c), it tends to draw out
609 some maxima that are not seen in the VISST retrievals. Again, this is due to the noisy retrieval
610 discussed earlier. Ideally, having an accurate independent measurement of the ice optical depth
611 during daytime would allow the retrieval of the liquid cloud optical depth underneath the ice
612 cloud and together yield a more accurate total optical depth and a better estimate of the CWP.
613 The results in CODIN3a suggest that its accuracy is currently insufficient for that application. It
614 should be noted that this example case uses a crude approximation to estimate τ_V simply for
615 demonstration, so any final conclusion about the efficacy of using ICODIN3a is unwarranted.
616 Perhaps, with further refinement it could be used to improve daytime retrievals of multiphase
617 and thick ice-over-water multilayered clouds using a method similar to that employed by *Minnis*
618 *et al.* [2007] to retrieve IWP from combined microwave LWP and imager retrievals of τ_{VISST}.
619

620 **6. Conclusions**

621 A neural network approach, ICODIN, using four combinations of thermal and shortwave
622 infrared wavebands has been developed to estimate opaque ice cloud optical depths at night, a
623 quantity heretofore ignored in passive infrared remote sensing due to the blackbody limit of
624 infrared emission. Clouds, especially those composed of ice crystals, are not true blackbodies,

625 but have detailed vertical structures in terms of ice water content, particle size and shape, water
626 vapor, and temperature that can affect the emitted radiances. Subtle changes in those components
627 related to the overall depth of the cloud as well as the radiating temperature of the cloud top can
628 potentially provide some information about the ice cloud optical depth. This potential is the
629 physical basis for the application of the neural network to this problem. Training of the ICODIN
630 used only 2 months of CloudSat data taken over the entire Earth. Even with no distinction
631 between air masses, surface types and temperatures, and cloud types, the ICODIN yields ice
632 cloud optical depths that are highly correlated, explaining 64% of the variance, with those from
633 the CloudSat radar-only algorithm and are unbiased, on average.

634 Application of the ICODIN requires initial screening of the data to identify opaque ice
635 clouds, which are those assumed to have optical depths greater than or equal to 8. The two
636 techniques, the BCH and SIST, used here greatly overestimate the frequency of opaque ice
637 clouds but the ICODIN successfully accounts for the semi-transparent cloud pixels by assigning
638 them appropriate values of τ. Using 4 channels (ICODIN4) produces the best overall agreement
639 with CloudSat, while the combination of 3.7, 11, and 12 μm (ICODIN3b) is the most promising
640 3-channel complement. The 3.7-μm channel is the one most sensitive to ice cloud optical depth.
641 When the ICODIN4 determines a cloud to have $\tau > 8$, the result is, on average, unbiased with
642 respect to CloudSat and has a relative standard error of ~72%. The relative error increases to
643 100% if clouds of all optical depths are included.

644 The training of the ICODIN here has relied on the CloudSat 2B-CWC-RO product, which is
645 known to have relatively large uncertainties that undoubtedly contribute to some of the error in
646 the ICODIN retrievals. Training with other IWC products (e.g., *Deng et al.* [2010], *Delanoë and*
647 *Hogan* [2010]) that include CALIPSO will likely yield similar results in a relative sense because

they are all closely correlated with the same in situ measurements [*Deng et al.* 2013]. Because CloudSat and CALIPSO are experimental satellites, their retrieval algorithms are periodically updated to improve the accuracy of the various parameters. Future research into neural networks for opaque cloud retrievals at night should explore the use of the alternative IWC retrievals as well as revisions of the 2B-CWC-RO product. Additionally, the radar-retrieved values of r_e should be analyzed to develop a means for computing IWP from τ_{CN} with the goal of estimating CWP for the subject cloud systems.

The analysis presented here has only begun the exploration of the ICODIN's potential. Reduction of uncertainties in the ICODIN may be possible by using a larger training dataset that incorporates data from all months of the year and possibly from additional years. The influence of the air mass, which may also impact the accuracy, could be taken into account by introducing additional input parameters such as the surface type and numerical weather analyses of surface temperature and temperature and humidity at selected levels. In the absence of a sensor having high precision for BT(3.7) < 220 K, it may be helpful to provide the algorithm with some indicator of the quality of the BT(3.7) value in order to downplay its influence at very low temperatures. An indicator of cloud type such as stratiform or convective might also be valuable as an input. With the implementation of these additional suggestions, it might be possible to significantly increase the technique's accuracy.

Only near-nadir measurements from MODIS were used in the development of the ICODIN. Thus, application of the method to satellite imager data will require understanding the dependence of the technique on VZA and may require training with other datasets, such as GOES or VIIRS, that provide a wide range of VZA views when matched with CloudSat. The examples shown here suggest that the VZA effect may be relatively small. Use of the technique

for other imagers such as VIIRS may require some means to account for differences in the spectral response functions such as spectral band adjustment factors that are based on hyperspectral data (e.g., *Scarino et al.* [2015]).

This study has definitively shown that the optical depth of ice clouds can be estimated with reasonable accuracy for clouds that are thicker than the "blackbody limit." While much additional analysis remains to be done, the development of the ICODIN approach opens up the potential for more accurate 24-h monitoring of clouds and for providing forecast models with estimates of cloud water path at all times of the diurnal cycle.

Acknowledgments. This research is supported by the NASA Modeling, Analysis, and Prediction Program and the NASA CERES Project.

References

Austin, R. T., A. J. Heymsfield, and G. L. Stephens (2009), Retrieval of ice cloud microphysical parameters using the CloudSat millimeter-wave radar and temperature, *J. Geophys. Res.*, *114*, D00A23, doi:10.1029/2008JD010049.

Chen, Y., H. Wang, J. Min, X.-Y. Huang, P. Minnis, R. Zhang, J. Haggerty, and R. Palikonda, (2015), Analysis of the cloud water component for WRF: Variational assimilation of cloud liquid/ice water path, *J. Appl. Meteorol. Climatol.*, *32*, doi:10.1175/JAMC-D-14-0243.1.

Delanoë, J. and R. J. Hogan (2010), Combined CloudSat–CALIPSO–MODIS retrievals of the properties of ice clouds, *J. Geophys. Res.*, *115*, D00H29, doi:10.1029/2009JD012346.

Deng, M., G. G. Mace, Z. Wang, and R. P. Lawson (2013), Evaluation of several A-Train ice cloud retrieval products with in situ measurements collected during the SPARTICUS campaign. *J. Appl. Meteor. Climatol*., *52*, 1014-1030, doi:10.1175/JAMC-D-12-054.1.

Deng, M., G. G. Mace, Z. Wang, and H. Okamoto (2010), Tropical Composition, Cloud and Climate Coupling Experiment validation for cirrus cloud profiling retrieval using CloudSat radar and CALIPSO lidar, *J. Geophys. Res.*, *115*, D00J15, doi:10.1029/2009JD013104.

Fridlind, A. M., A. S. Ackerman, J.-P. Caboreau, J. Fan, W. W. Grabowski, A. Hill, T. R. Jones,

M. M. Khaiyer, G. Liu, P. Minnis, H. Morrison, L. Nguyen, S. Park, J. C. Petch, J. P. Pinty, C. Schumacher, B. Shipway, A. C. Varble, X. Wu, S. Xie, and M. Zhang (2012), A comparison of TWP-ICE observational data with cloud-resolving model results, *J. Geophys. Res.*, *117*, D5, doi:10.1029/2011JD016595.

Heidinger, A. K. (2003), Rapid daytime estimation of cloud properties over a large area from radiance distributions, *J. Atmos. Oceanic Technol.*, *20*, 1237–1250.

Hillger, D. *et al.* (2013), First-light imagery from Suomi NPP VIIRS, *Bull. Amer. Meteor. Soc.*, *94*, 1019–1029.

Hong, G., P. Yang, A. K. Heidinger, M. J. Pavolonis, B. A. Baum, and S. E. Platnick (2010a), Detecting opaque and nonopaque tropical upper tropospheric ice clouds: A trispectral technique based on the MODIS 8–12 μm window bands, *J. Geophys. Res.*, *115*, doi:10.1029/2010JD014004.

Hong, G., P. Minnis, J. K. Ayers, C. R. Yost, and W. L. Smith, Jr. (2010b), Nighttime retrievals of cloud properties from infrared radiances at 3.7, 6.7, 11.0, and 12.0 μm, *AMS 17th Conf. Satellite Meteorology & Oceanography*, Annapolis, MD, Sept. 27-30, P1.10. [Available online at http://www-pm.larc.nasa.gov/site/doc-library/259-AMS_2010_17th.pdf]

Hong, G., P. Minnis, W. L. Smith, Jr., S. Sun-Mack, J. K. Ayers, C. R. Yost, and Y. Chen, (2012), Non-opaque and opaque ice cloud properties from infrared radiances at 3.7, 6.7, 11.0, and 12.0 μm, *2012 Intl. Radiation Symp.*, Berlin, Germany, 6-10 August, IRS2012-491-2. [Available online at http://www-pm.larc.nasa.gov/site/doc-library/258-IRS2012_Hong.pdf]

Huang, H.-L., P. Yang, H. Wei, B. A. Baum, Y. X. Hu, P. Atonelli, and S. A. Ackerman (2004), Inference of ice cloud properties from high spectral resolution infrared observations, *IEEE Trans. Geosci. Remote Sens.*, *42*, 842–852.

Im, E., S. L. Durden, and C. Wu, (2005), Cloud profiling radar for the CloudSat mission, *IEEE Trans. Aerosp. Electron. Syst.*, *20*, 15–18, doi:10.1109/MAES.2005.1581095.

Inoue, T. (1985), On the temperature and effective emissivity determination of semi-transparent cirrus clouds by bispectral measurements in the 10 micron window region, *J. Meteor. Soc. Japan*, *63*, 88–99.

Jones, T. A., K. Knopfmeier, D. Wheatley, G. Creager, P. Minnis, and R. Palikonda (2015a), Storm-scale data assimilation and ensemble forecasting with the NSSL Experimental Warn-

728 on Forecast. Part 2: Combined radar and satellite data experiments, *Wea. Forecasting*,
729 submitted.
730 Jones, T. A., D. J. Stensrud, P. Minnis, and R. Palikonda (2013), Evaluation of a forward
731 operator to assimilate cloud water path into WRF-DART, *Mon. Wea. Rev.*, *141*, 2272-2289,
732 doi:10.1175/MWR-D-12-00238.1.
733 Jones, T. A., D. J. Stensrud, L. Wicker, P. Minnis, and R. Palikonda (2015a), Simultaneous radar
734 and satellite data storm-scale assimilation using an ensemble Kalman filter approach for 24
735 May 2011, *Mon. Wea. Rev.*, *143*, 165-194, doi:10.1175/MWR-D-14-00180.1.
736 Karayiannis, N. B. and A. N. Venetsanopoulos (1993), Efficient learning algorithms for neural
737 networks (ELEANNE), *IEEE Trans. Systems, Man, Cybernetics*, *23*, 1372-1383.
738 Kato, S., S. Sun-Mack, W. F. Miller, F. G. Rose, Y. Chen, P., Minnis, and B. A. Wielicki (2010),
739 Relationships among cloud occurrence frequency, overlap, and effective thickness derived
740 from CALIPSO and CloudSat merged cloud vertical profiles, *J. Geophys. Res.*, *115*,
741 D00H28, doi:10.1029/2009JD012277.
742 Kato, S., et al. (2011), Improvements of top-of-atmosphere and surface irradiances with
743 CALIPSO, CloudSat, and MODIS-derived cloud and aerosol properties, *J. Geophys. Res*.,
744 ***116***, D19209, doi:10.1029/2011JD016050.
745 King, M. D., et al. (2003), Cloud and aerosol properties, precipitable water, and profiles of
746 temperature and water vapor from MODIS, *IEEE Trans. Geosci. Remote Sens.*, *41*, 442–458.
747 Kox, S., L. Bugliaro, and A. Ostler (2014), Retrieval of cloud optical thickness and top altitude
748 from geostationary remote sensing, *Atmos. Meas. Tech.*, *7*, 3233-3246, doi:10.5194/amt-7-
749 3233-2014.
750 Lin, X. and J. Coakley, Jr. (1993), Retrieval of properties for semitransparent clouds from
751 multispectral infrared imagery data, *J. Geophys. Res.*, *98*, 18501–18514.
752 Liou, K.-N., S. C. Ou, Y. Takano, F. P. J. Valero, and T. P. Ackerman (1990), Remote sounding
753 of the tropical cirrus cloud temperature and optical depth using 6.5 and 10.5 μm radiometers
754 during STEP, *J. Appl. Meteorol.*, *29*, 716–726.
755 McGill, M. J., L. Li, W. D. Hart, G. M. Heymsfield, D. L. Hlavka, P. E. Racette,L. Tian, M. A.
756 Vaughan, and D. M. Winker (2004), Combined lidar-radar remote sensing: Initial results
757 from CRYSTAL-FACE, *J. Geophys. Res.*, *109*, D07203, doi:10.1029/2003JD004030.
758 Miller, S. D. and R. E. Turner (2009), A dynamic lunar spectral irradiance data set for

759 NPOESS/VIIRS day/night band nighttime environmental applications, *IEEE Trans. Geosci.*
760 *Remote Sens.*, *47*, 2316-2329.
761 Menzel, W. P., R. A. Frey, B. A. Baum, and H. Zhang (2006), MODIS cloud top properties and
762 cloud phase algorithm theoretical basis document,
763 http://modis.gsfc.nasa.gov/data/atbd/atbd_mod04.pdf.
764 Minnis, P., G. Hong, W. L. Smith, Jr., and P. W. Heck, 2010: Cloud optical depths at night:
765 Going beyond the infrared blackbody limits. *2010 NOAA STAR AWG/RRR-Review*, Madison,
766 WI, June 7-11. [Available online at http://www-pm.larc.nasa.gov/site/doc-library/256-
767 Minnis.poster.AWG.10.pdf]
768 Minnis, P., G. Hong, J. K. Ayers, W. L. Smith, Jr., S. Sun-Mack, C. R. Yost, Y. Chen, and P. W.
769 Heck, 2011a: Enhanced nighttime cloud retrievals. *2011 NOAA STAR GOES-R AWG Ann.*
770 *Rev.*, Ft. Collins, CO, June 14-16. [Available online at http://www-pm.larc.nasa.gov/site/doc-
771 library/257-Minnis.poster.AWG.11.pdf]
772 Minnis, P., et al. (2012), Simulations of infrared radiances over a deep convective cloud system
773 observed during TC4: Potential for enhancing nocturnal ice cloud retrievals. *Remote Sens.*, *4*,
774 3022-3054, doi:10.3390/rs4103022.
775 Minnis, P., J. Huang, B. Lin, Y. Yi, R. F. Arduini, T.-F. Fan, J. K. Ayers, and G. G. Mace
776 (2007), Ice cloud properties in ice-over-water cloud systems using TRMM VIRS and TMI
777 data. *J. Geophys. Res.*, *112*, D06206, doi:10.1029/2006JD007626.
778 Minnis, P., et al. (2008), Near-real time cloud retrievals from operational and research
779 meteorological satellites, *Proc. SPIE Europe Remote Sens. 2008*, Cardiff, Wales, UK, 15-18
780 September, *7107-2*, 8 pp. [Available online at http://www-pm.larc.nasa.gov/site/doc-
781 library/99-Minnis.etal.SPIE.abs.08.pdf]
782 Minnis, P., et al. (2011b), CERES Edition-2 cloud property retrievals using TRMM VIRS and
783 Terra and Aqua MODIS data, Part I: Algorithms, *IEEE Trans. Geosci. Remote Sens.*, *49*,
784 4374-4400.
785 Minnis, P., et al. (2010), CERES Edition 3 cloud retrievals, *AMS 13th Conf. Atmos. Rad.*,
786 Portland, OR, June 27 – July 2, 5.4. [Available online at
787 https://ams.confex.com/ams/pdfpapers/171366.pdf]
788 NASA, 2015: CERES Terra & Aqua Edition 4a SSF Cloud Properties – Accuracy and
789 Validation. CERES Technical Report, 43 pp., August 15. [Available online at http://www-

790 pm.larc.nasa.gov/site/doc-library/260-ssf_cloud_prop_aqua_ed4.cal_val.pdf]
791 Norris, P. M, and A. M. da Silva (2015), Monte Carlo Bayesian inference on a statistical model
792 of sub-grid column moisture variability using high-resolution cloud observations. Part I:
793 Sensitivity tests and results, *Q. J. Roy. Meteorol. Soc.*, submitted.
794 Ou, S.C., K.-N. Liou, W. M. Gooch, and Y. Takano (1993), Remote sensing of cirrus cloud
795 properties using Advanced Very-High Resolution Radiometer 3.7 and 10.9-μm channels,
796 *Appl. Opt.*, *32*, 2171–2180.
797 Scarino, B. R., D. R. Doelling, P. Minnis, A. Gopalan, T. Chee, R. Bhatt, and C. Lukashin, 2015:
798 An online interface for calculating spectral band difference adjustment factors derived from
799 SCIAMACHY data. *IEEE Trans. Geosci. Remote Sens.*, accepted.
800 Smith, W. L., Jr. (2014), 4-D cloud properties from passive satellite data and applications to
801 resolve the flight icing threat to aircraft, *Ph.D. Dissertation*, Univ. Wisconsin-Madison,
802 Madison, WI, 165 pp. [http://www-pm.larc.nasa.gov/icing/pub/WLS-Dissertation.pdf]
803 Smith, W. L., Jr., P. Minnis, C. Fleeger, M. Khaiyer, D. Spangenberg, R. Palikonda, 2015: An
804 empirical profiling method to improve the resolution of cloud ice and liquid water content
805 using satellite imager data. Submitted to *J. Appl. Meteor. Climatol.*
806 Stephens, G. L., et al. (2002), The CloudSat mission and A-Train, *Bull. Am. Meteorol. Soc*., *83*,
807 1771–1790.
808 Stephens, G. L., et al. (2008), CloudSat mission: Performance and early science after the first
809 year of operation, *J. Geophys. Res.*, *113*, D00A18, doi: 10.1029/2008JD009982.
810 Szejwach, G. (1982), Determination of semi-transparent cirrus cloud temperature from infrared
811 radiances: Application to Meteosat, *J. Appl. Meteorol.*, *21*, 384-393.
812 Tian, B., B. J. Soden, and X. Wu (2004), Diurnal cycle of convection, clouds, and water vapor in
813 the tropical upper troposphere: Satellites versus a general circulation model, *J. Geophys.*
814 *Res.*, *109*, D10101, doi:10.1029/2003JD004117.
815 Walther, A., A. K. Heidinger, and S. Miller (2013), The expected performance of cloud optical
816 and microphysical properties derived from Suomi NPP VIIRS day/night band lunar
817 reflectance, *J. Geophys. Res*., *118*, 13230-13240, doi:10.1002/2013JD020478.
818 Winker, D. M., W. H. Hunt, and M. J. McGill (2007), Initial performance assessment of
819 CALIOP, *Geophys. Res. Lett.*, *34*, L19803, doi:10.1029/2007GL030135.
820 Yue, Q., and K.-N. Liou (2009), Cirrus cloud optical and microphysical properties determined

821 from AIRS infrared spectra, *Geophys. Res. Lett.*, *36*, L05810, doi:10.1029/2008GL036502.

Table 1. Correlation and differences between ICODIN and CPR ice cloud optical depths.

Method	Year	Mean	R	Bias	Bias (%)	SDD	SDD (%)
ICODIN4	2007	8.85	0.80	-0.07	-0.8	8.73	99
3.7, 6.7, 11, 12 μm	2008	8.50	0.78	-0.10	-1.2	8.89	105
ICODIN3a	2007	8.95	0.79	-0.05	-0.6	9.20	103
6.7, 11, 12 μm	2008	8.60	0.75	-0.07	-0.8	9.45	110
ICODIN3b	2007	8.83	0.79	-0.09	-1.0	8.91	101
3.7, 11, 12 μm	2008	8.51	0.78	-0.10	-1.2	8.94	105
ICODIN3c	2007	8.86	0.80	-0.05	-0.6	8.80	99
3.7, 6.7, 11 μm	2008	8.51	0.77	-0.10	-1.2	9.13	107

Table 2. Same as Table 1, except for all pixels with $\tau_{CS} \geq 8$.

Method	Year	Mean	R	Bias	Bias (%)	SDD	SDD (%)
ICODIN4	2007	18.6	0.72	-3.7	-19.9	14.2	76.3
3.7, 6.7, 11, 12 μm	2008	18.1	0.69	-3.95	-21.8	14.7	81.2
ICODIN3a	2007	18.0	0.72	-4.5	-25.0	14.7	81.7
6.7, 11, 12 μm	2008	17.4	0.68	-4.8	-27.5	15.3	87.9
ICODIN3b	2007	18.3	0.71	-4.0	-21.9	14.4	78.7
3.7, 11, 12 μm	2008	17.9	0.69	-4.1	-22.9	14.7	82.1
ICODIN3c	2007	18.5	0.72	-3.8	-20.5	14.3	77.3
3.7, 6.7, 11 μm	2008	18.0	0.77	-4.1	-22.8	15.1	83.9

Table 3. Same as Table 1, except for all pixels with $\tau_{CN} \geq 8$.

Method	Year	Mean	R	Bias	Bias (%)	SDD	SDD (%)
ICODIN4	2007	19.7	0.73	-0.05	-0.2	14.0	71.1
3.7, 6.7, 11, 12 μm	2008	19.5	0.69	-0.04	-0.2	14.5	74.3
ICODIN3a	2007	19.3	0.71	-0.04	-0.2	14.5	75.1
6.7, 11, 12 μm	2008	19.0	0.67	0.08	0.4	15.2	80.0
ICODIN3b	2007	19.6	0.72	0.02	0.1	14.2	72.4
3.7, 11, 12 μm	2008	19.5	0.69	0.09	0.5	14.5	74.3
ICODIN3c	2007	20.1	0.72	0.00	0.0	14.3	71.1
3.7, 6.7, 11 μm	2008	19.9	0.66	-0.05	-0.3	15.2	76.4

Table 4. Frequency (%) of cloud thickness category, CODIN4 system vs. CloudSat. Original opaque indicates the fraction of pixels classified by BCH or SIST as opaque.

Method	BCH				SIST			
# samples	1.7×10^6				1.1×10^6			
Year	2007		2008		2007		2008	
Category	$\tau_{CS} < 8$	$\tau_{Cs} \geq 8$	$\tau_{CS} < 8$	$\tau_{CS} \geq 8$	$\tau_{CS} < 8$	$\tau_{CS} \geq 8$	$\tau_{CS} < 8$	$\tau_{CS} \geq 8$
$\tau_{CN4} < 8$	59.0	7.0	60.4	7.2	35.3	2.8	35.7	3.0
$\tau_{CN4} \geq 8$	8.8	25.2	8.6	23.8	13.1	48.5	13.3	48.0
Original opaque	67.8	32.2	69.0	31.0	48.4	51.3	49	51

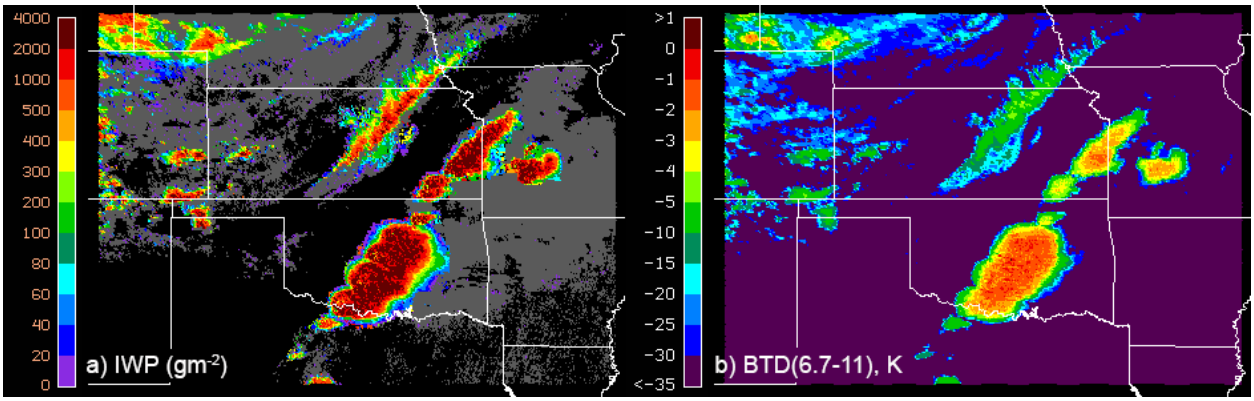

Figure 1. Parameters derived from GOES-13 over southern Great Plains, 2015 UTC, 20 May 2013. (a) Ice water path, (b) brightness temperature difference between 6.7 and 11 μm channels.

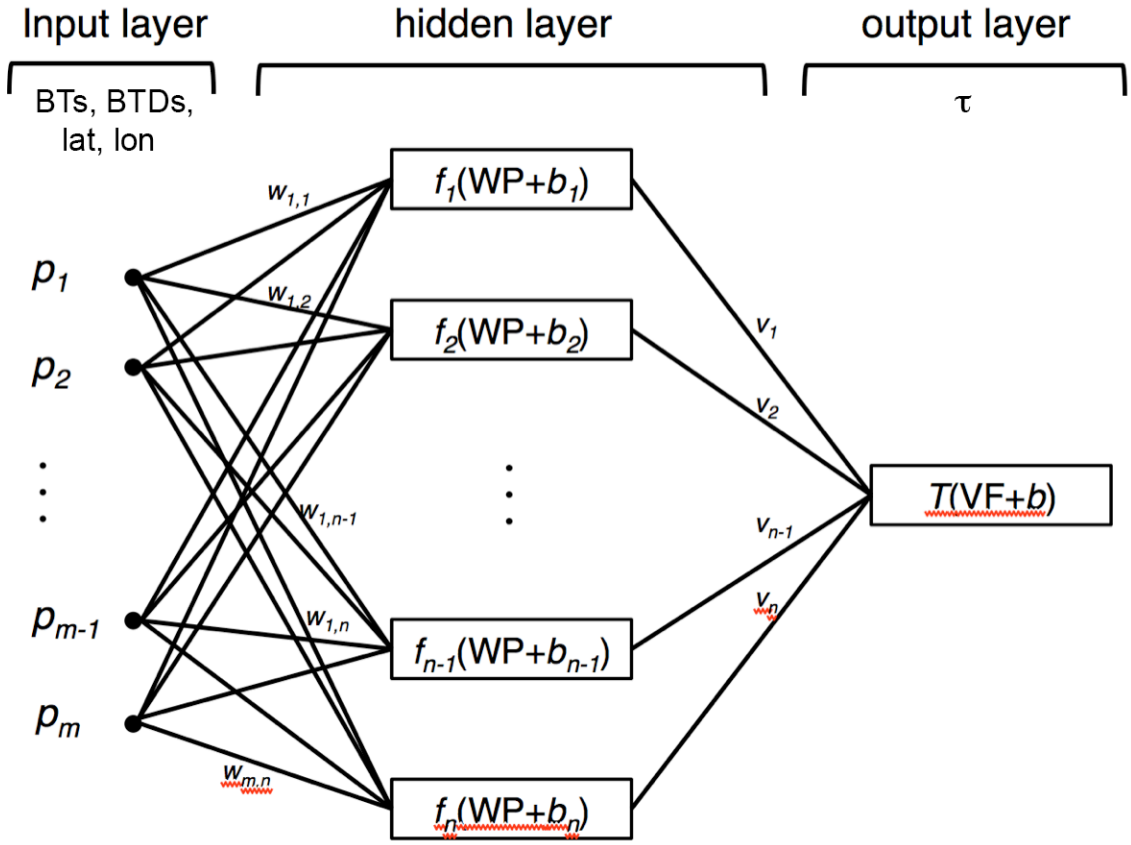

Figure 2. Schematic diagram of three-layer neural network used to determine opaque ice cloud visible optical depth τ.

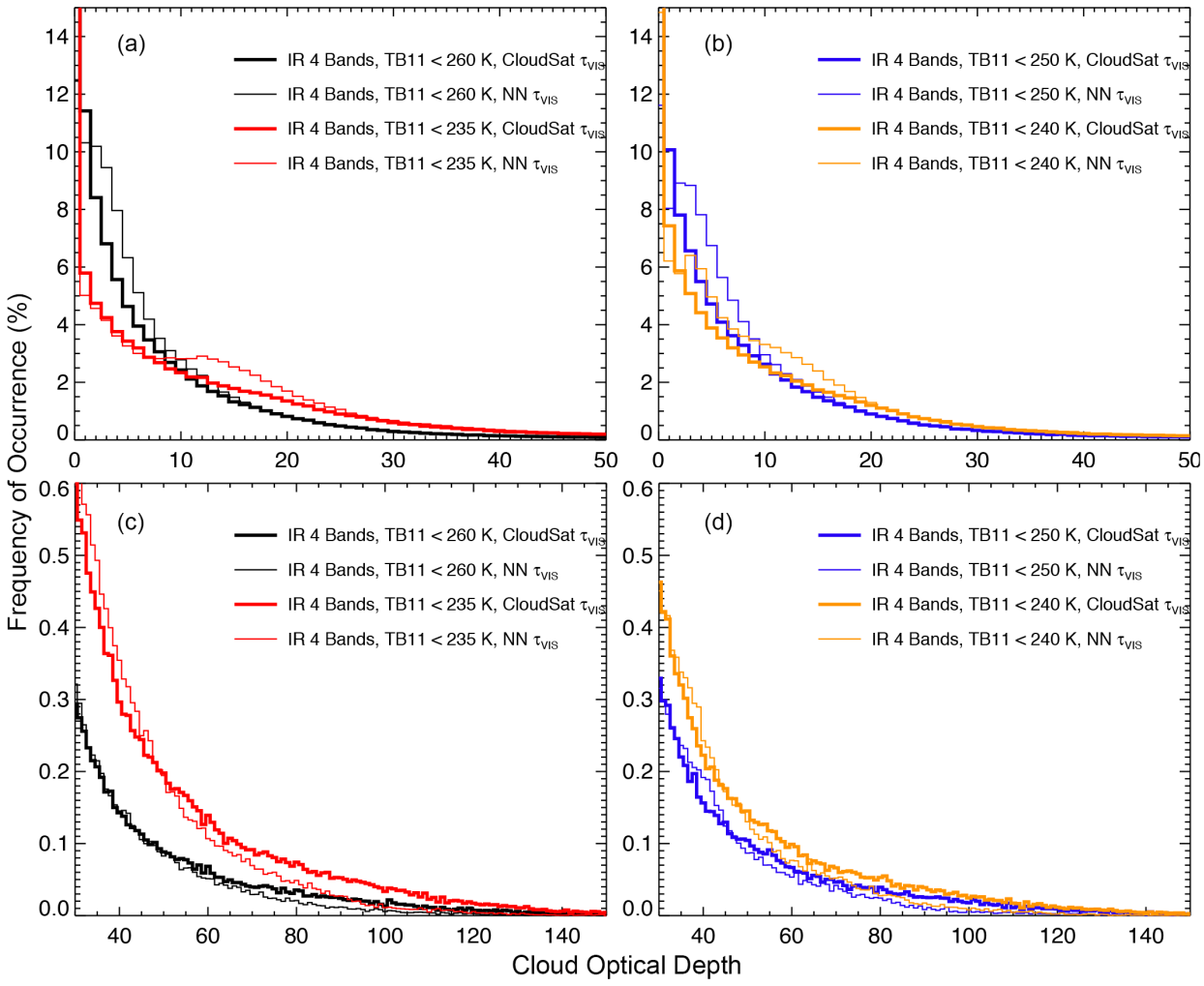

Figure 3. Probability distributions of 2007 global τ values retrieved from CloudSat data and from Aqua MODIS using ICODIN4 with four observed 11-μm brightness temperature thresholds. (bin size = 1).

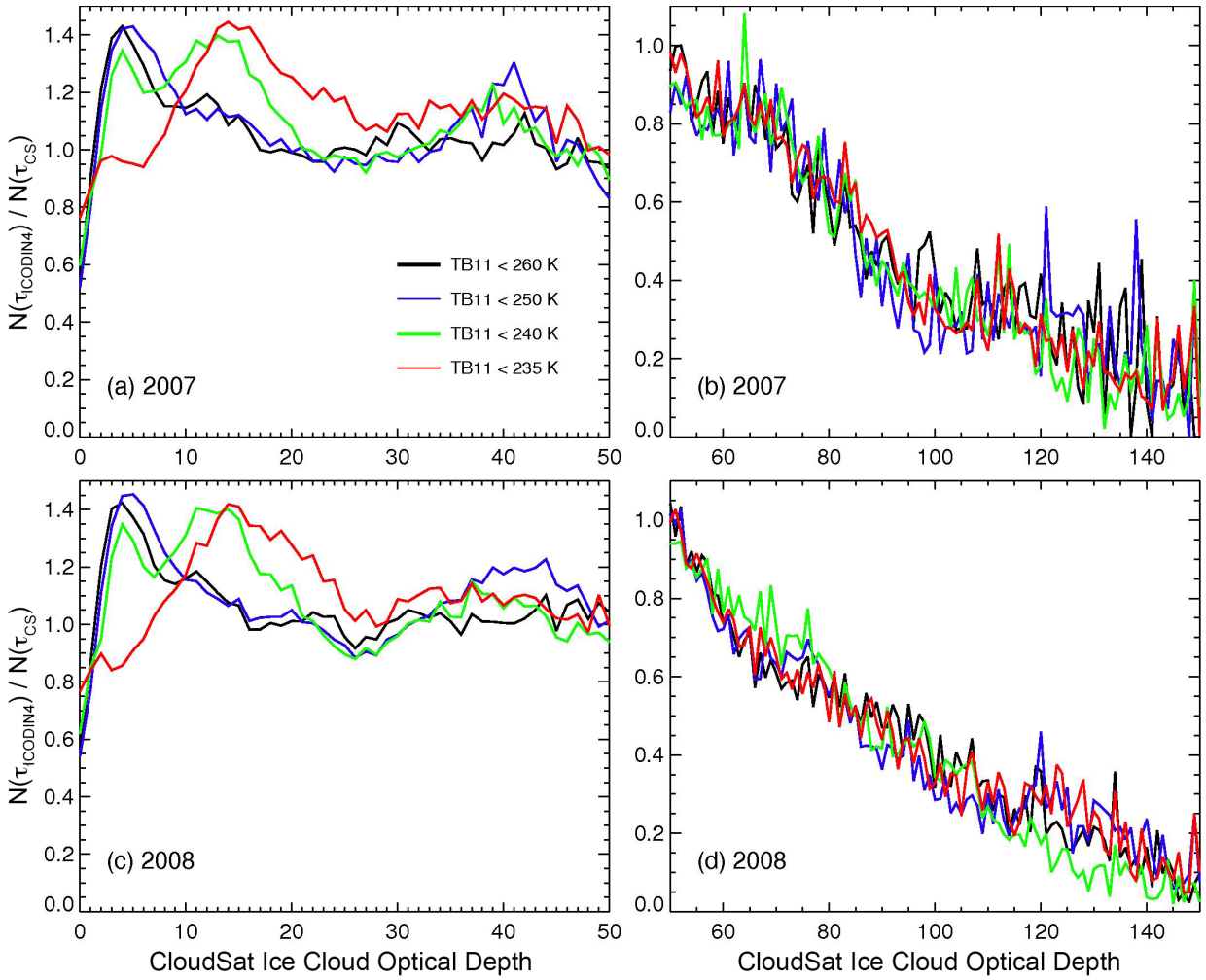

Figure 4. Ratio of occurrence frequencies of ICODIN4 optical depth to those of CloudSat optical depth for a given CloudSat ice cloud optical depth. Note scale difference between left and right panels. Left panels for $\tau \leq 50$, right panels for $\tau > 50$.

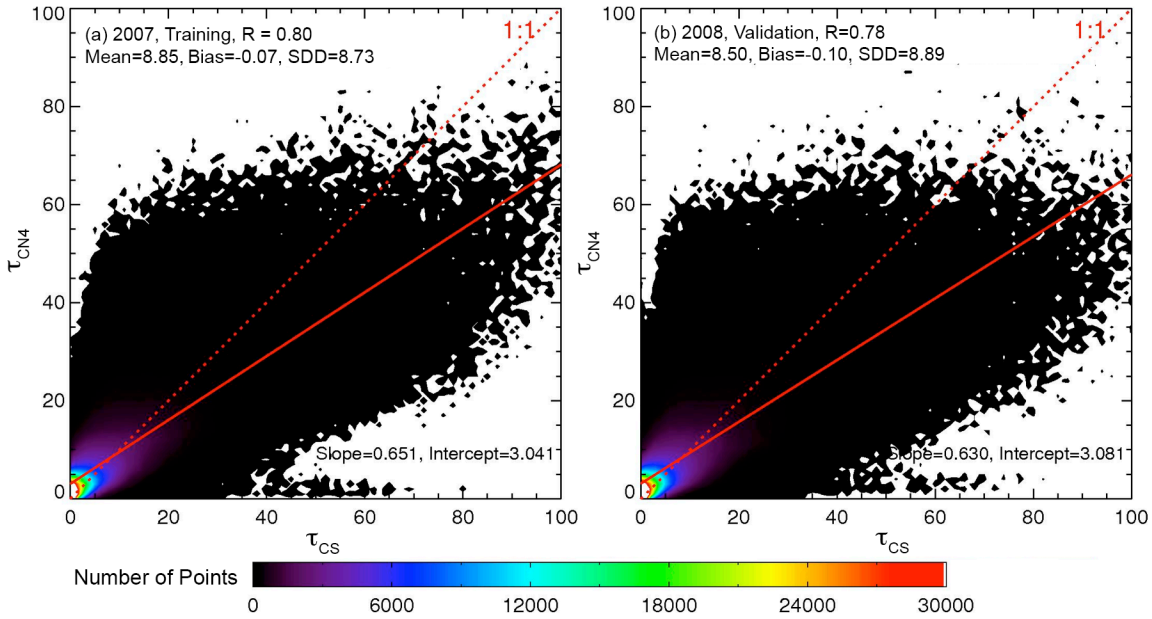

Figure 5. Density scatterplots of nocturnal opaque ice cloud optical depths retrieved from CloudSat and Aqua MODIS data using ICODIN4 from (a) the training period, 2007, and (b) the validation period, 2008.

71

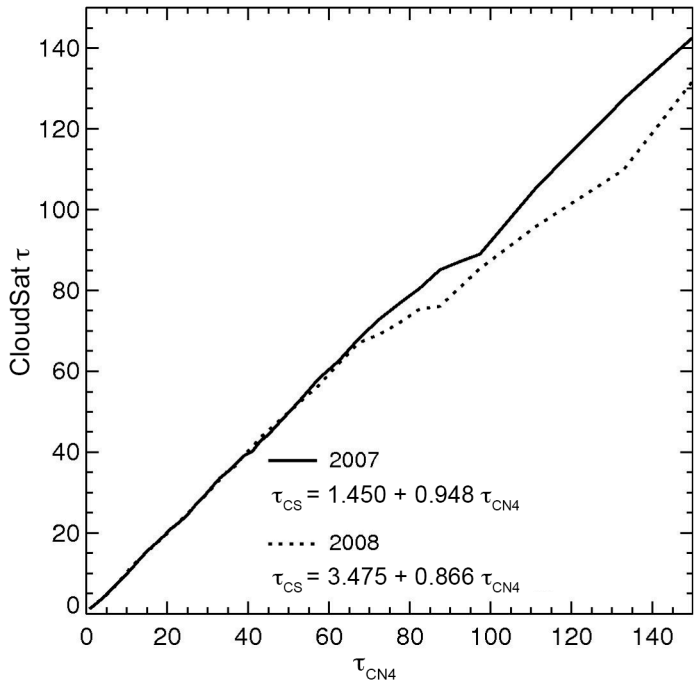

72

73 Figure 6. Mean bin opaque ice cloud optical depth from CPR retrieval as a function of ICODIN4
74 optical depth from 2007 training (solid) and 2008 validation results (dashed). Each bin
75 corresponds to 2.5 ($\tau_{CN4} < 50$) and 5 ($\tau_{CN4} \geq 50$) ICODIN4 optical depth units.
76

77
78

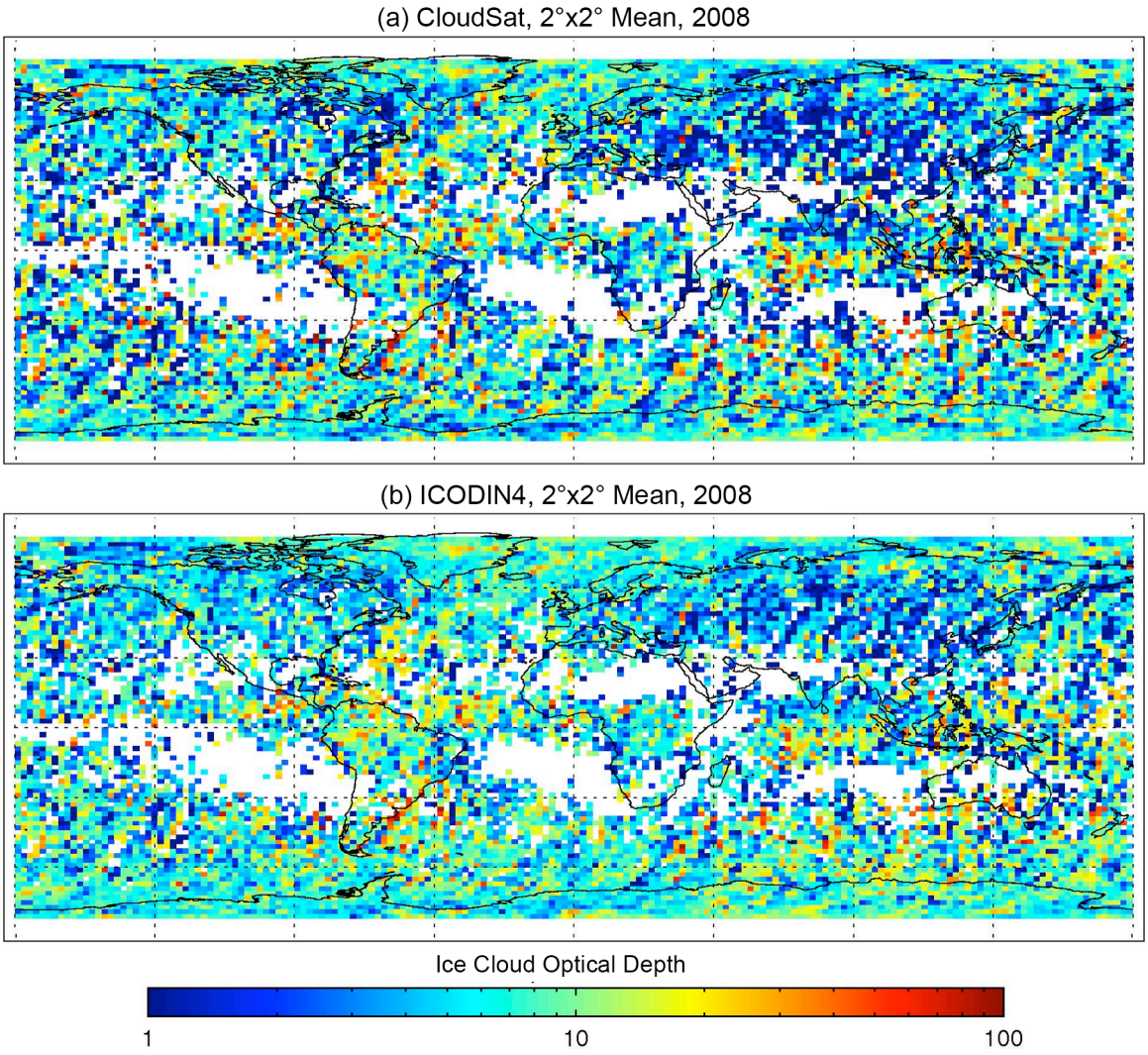

79

80 Figure 7. Geographical distribution of 2°x2° regional mean opaque ice cloud optical thickness
81 during nighttime in 2008 from (a) CloudSat CPR retrievals and (b) Aqua MODIS ICODIN4
82 retrievals.

83

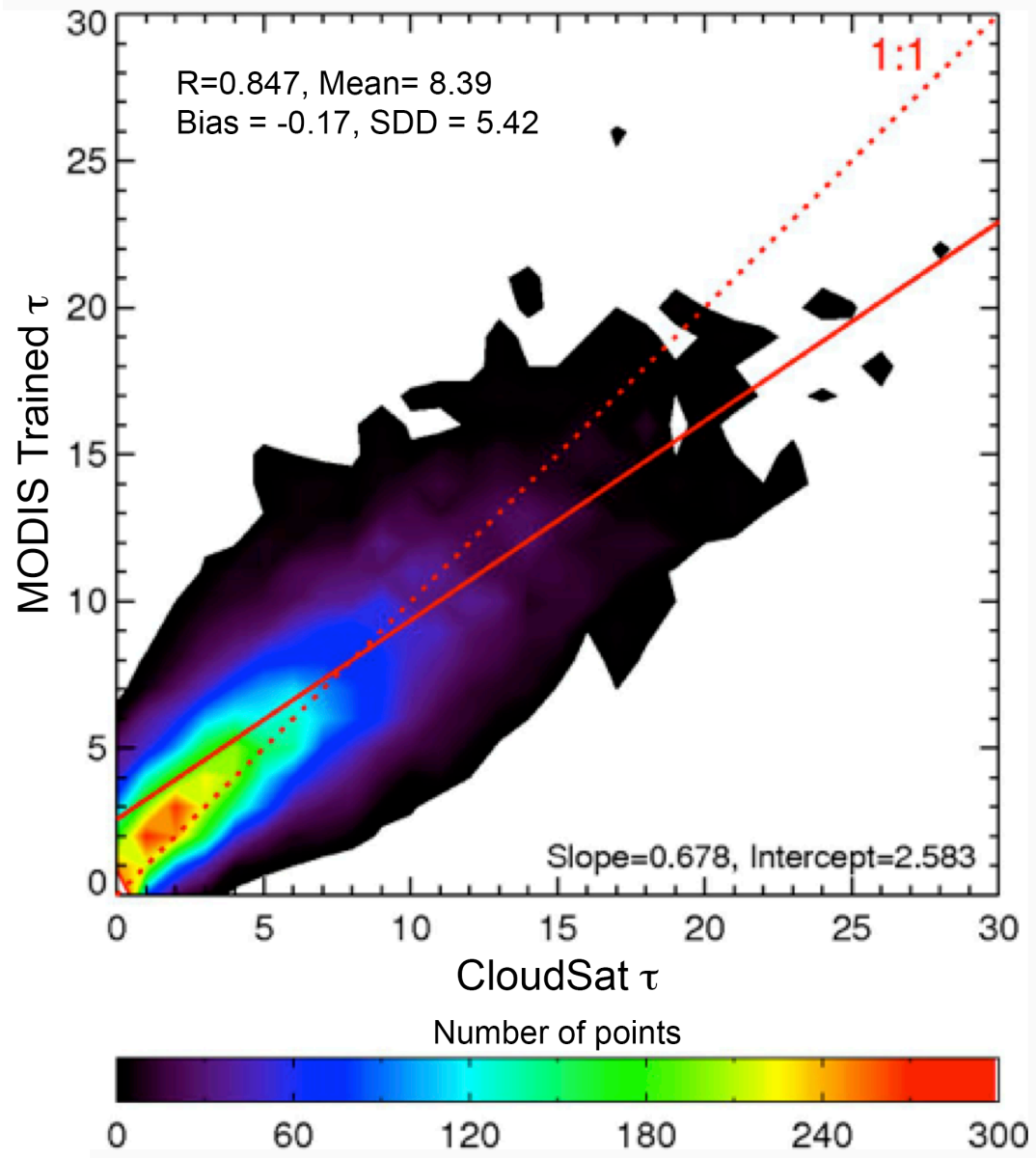

Figure 8. Density plots of the correlation between 2008 2°x2° regional mean τ estimated from data in Figure 5 (bin size = 1).

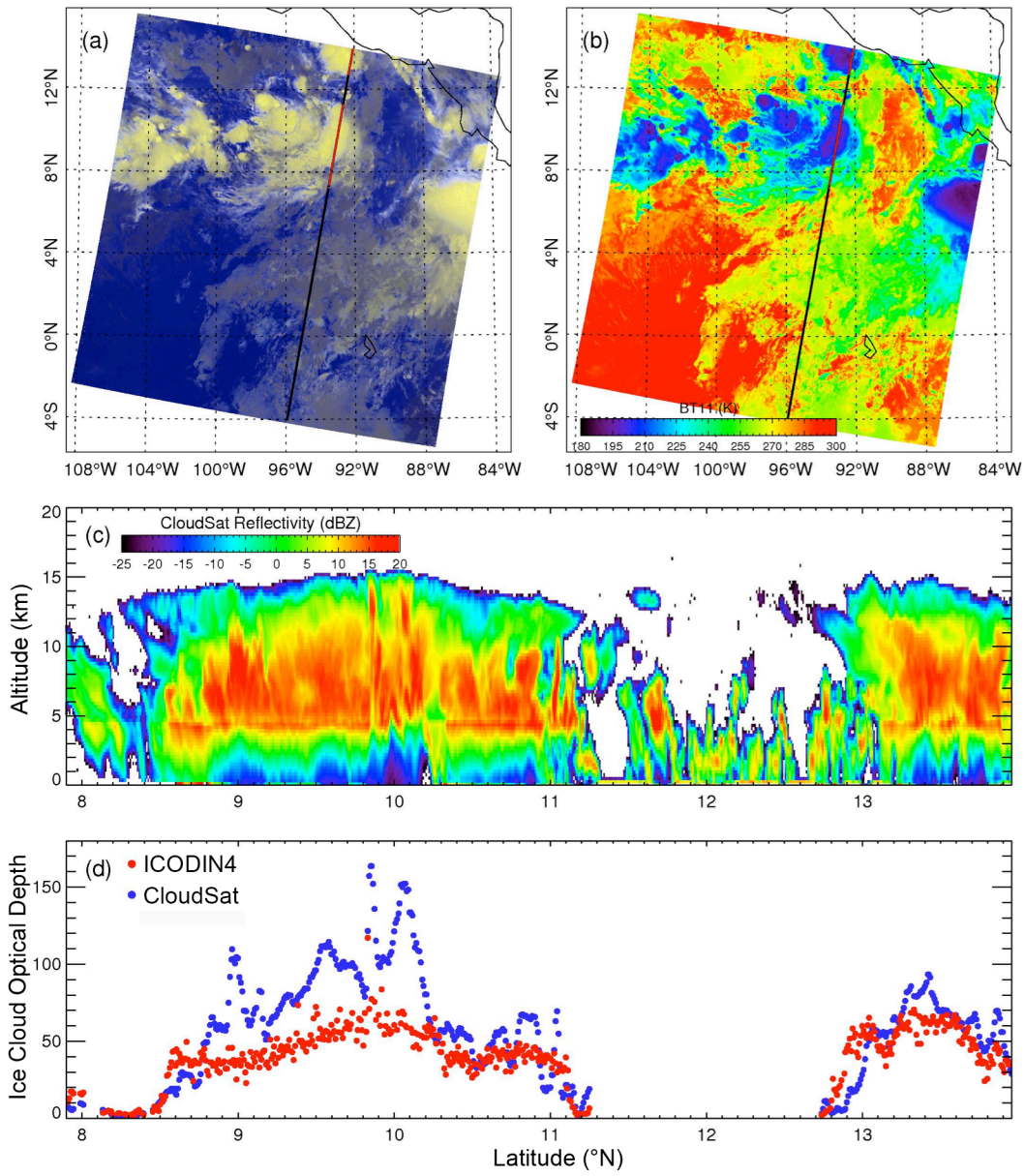

Figure 9. Example of matched Aqua MODIS and CloudSat CPR data and retrievals over eastern tropical Pacific Ocean (108°W-84°W, 4°S-15°N), 0800 UTC, 6 June 2008. (a) MODIS granule RGB [Red: Inverted BT(11), Green: Inverted BT(12), Blue: BTD(11-12)] image with overlay of CloudSat ground track as black and red (showing opaque ice clouds) line, (b) MODIS BT(11) with CloudSat ground track, (c) CPR reflectivity along a track segment, and (d) estimated optical thickness from CloudSat (blue) and ICODIN4 for opaque ice clouds (red).

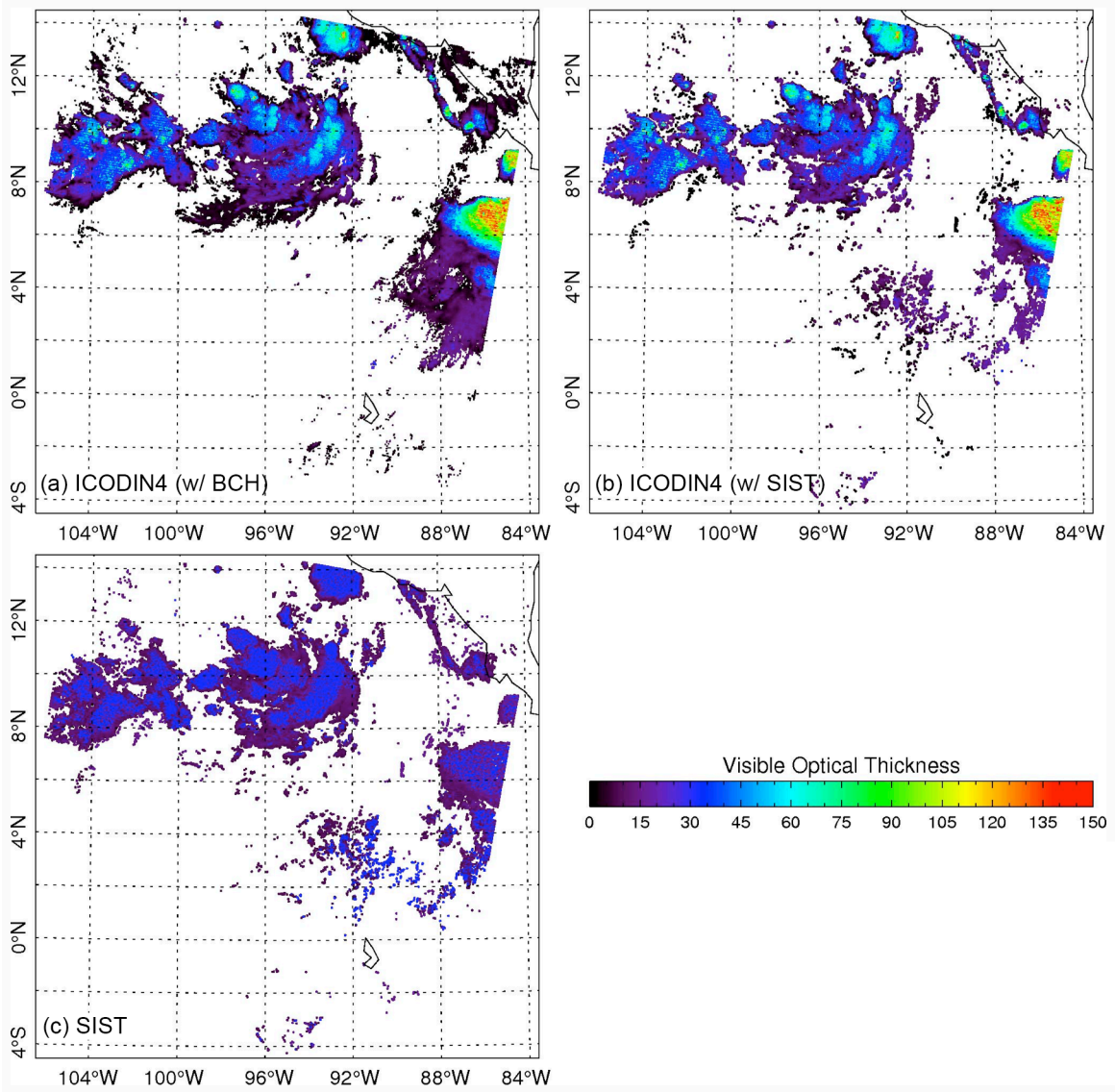

Figure 10. Estimated opaque ice cloud optical thickness for Aqua MODIS granule (see Figures 9a, b) at 0800 UTC, 6 June 2008. τ_{CN4} from ICODIN4 (3.7, 6.7, 11.0, and 12.0 μm) using (b) BCH and (c) SIST to identify opaque ice clouds. and (c) from CERES Edition-4 SIST retrievals using SIST retrievals or default values for opaque ice clouds.

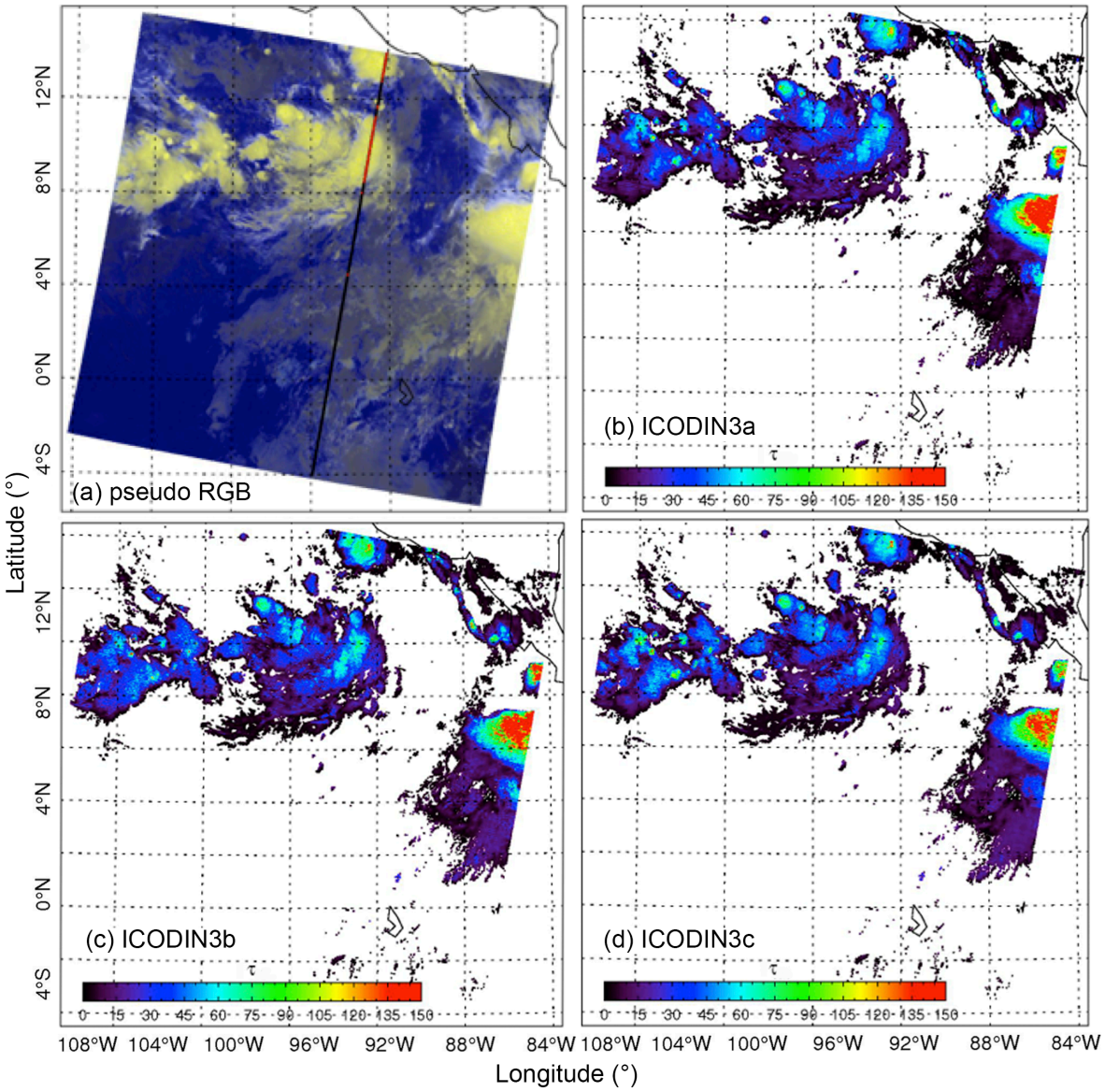

Figure 11. Same as Figure 10, except for (b) τ_{CN3a} from ICODIN3a (6.7, 11.0, and 12.0 μm) and (c) τ_{CN3b} from ICODIN3b (3.7, 11.0, and 12.0 μm), and (d) τ_{CN3c} from ICODIN3c (3.7, 6.7, and 11.0). The BCH method was used in all cases to identify opaque ice cloud pixels.

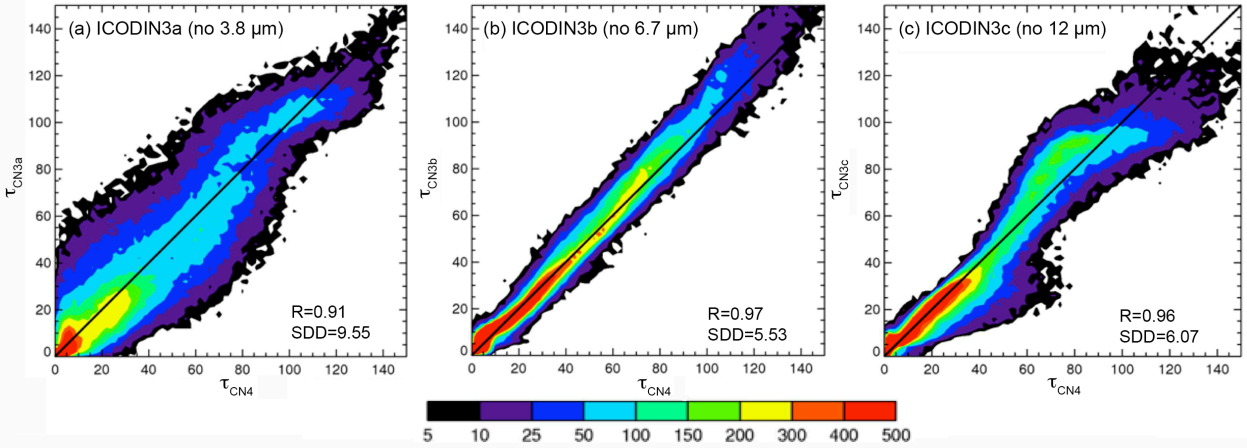

Figure 12. Comparisons of "opaque" ice cloud optical thickness from three-channel methods with that, τ_{CN4}, from four-channel technique (ICODIN4) for the MODIS granule in Figure 7. (a) τ_{CN3a} from ICODIN3a (6.7, 11.0, and 12.0 μm) and (b) τ_{CN3b} from ICODIN3b (3.7, 11.0, and 12.0 μm), and (d) τ_{CN3c} from ICODIN3c (3.7, 6.7, and 11.0).

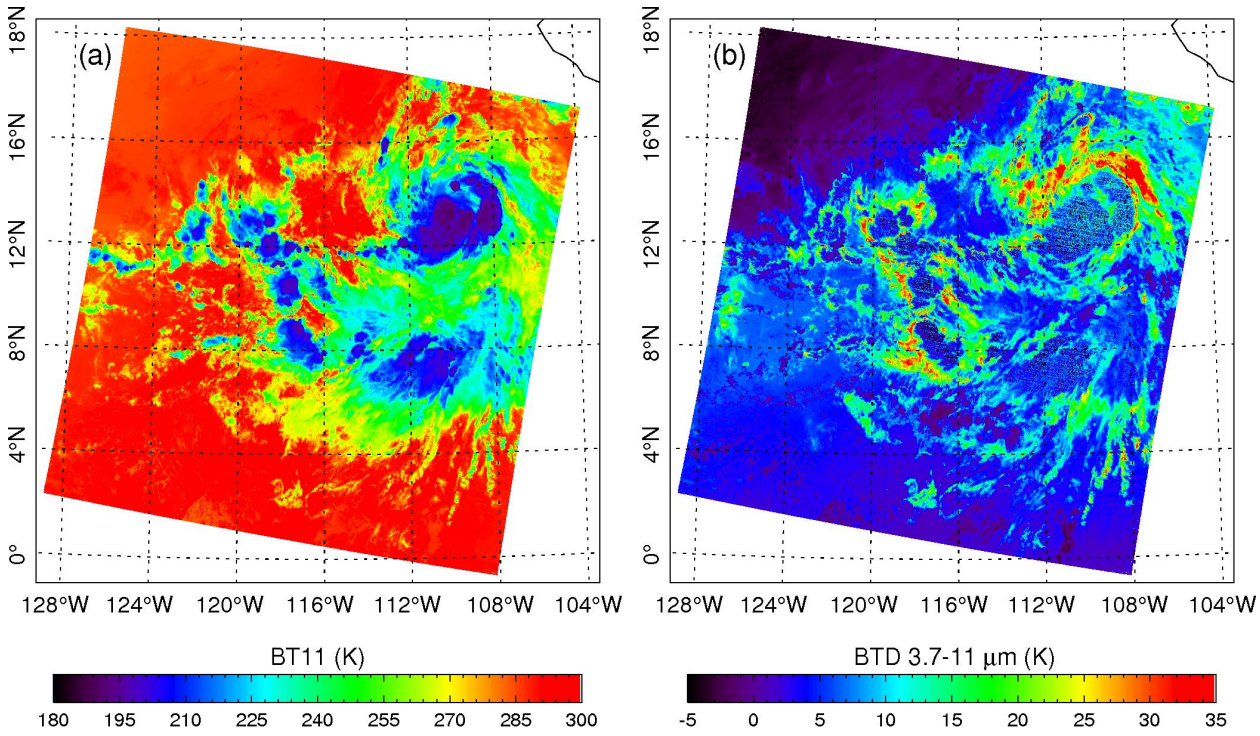

Figure 13. Aqua MODIS image at night over the eastern Pacific at 0925 UTC, 5 July 2012, (a) BT(11) and (b) BTD(3.7-11).

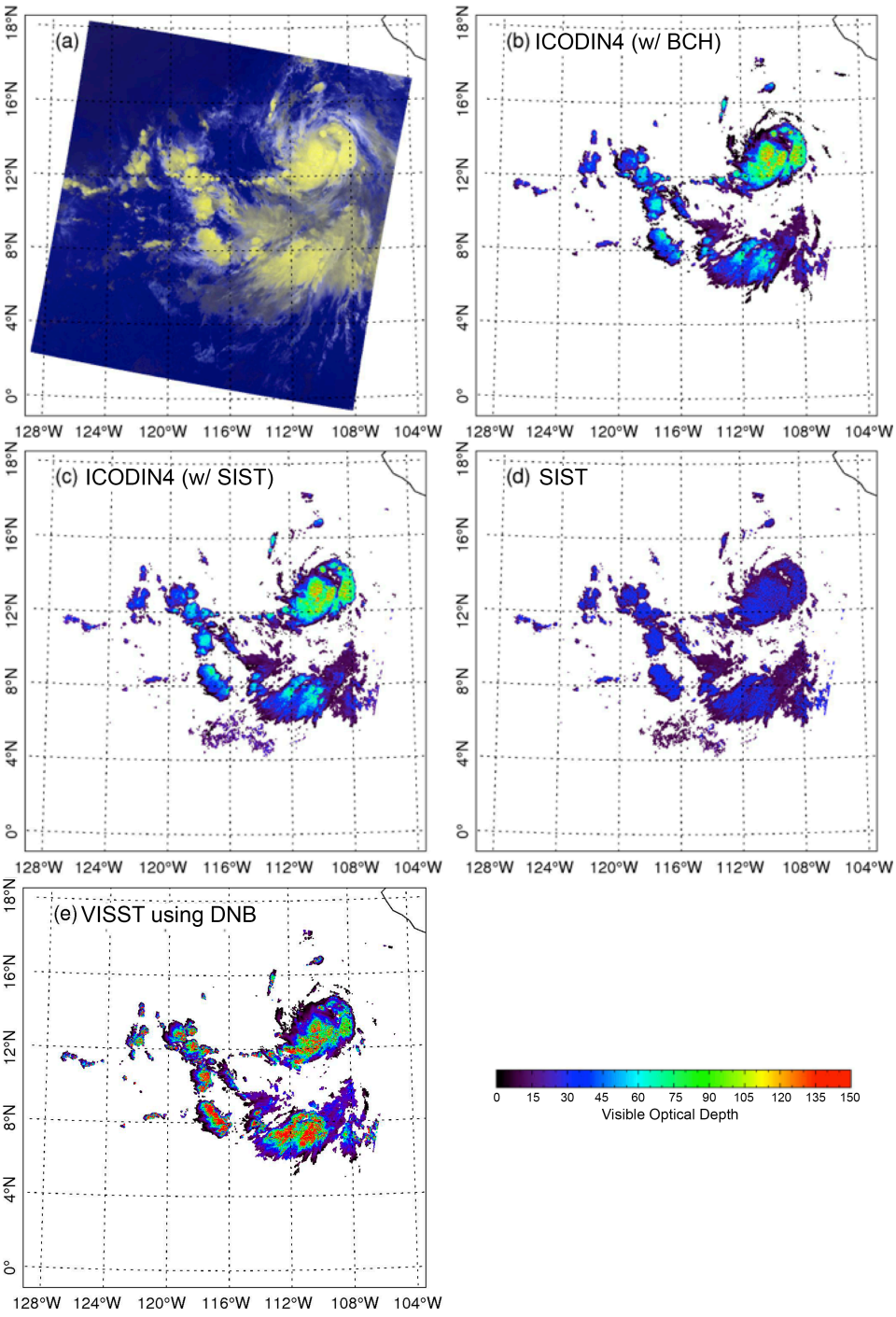

Figure 14. Opaque ice cloud optical depths estimated using three methods at night over the eastern Pacific at 0925 UTC, 5 July 2012. (a) Aqua MODIS RGB [Red: inverted BT(11), Green: inverted BT(12), Blue: BTD(3.7-11)]; τ_{CN4} estimated from ICODIN4 applied to Aqua MODIS data with (b) BCH and (c) SIST selection of opaque clouds, (d) τ estimated from SIST method, (e) opaque ice cloud τ estimated from DNB retrieval applied to matching SNPP VIIRS data.

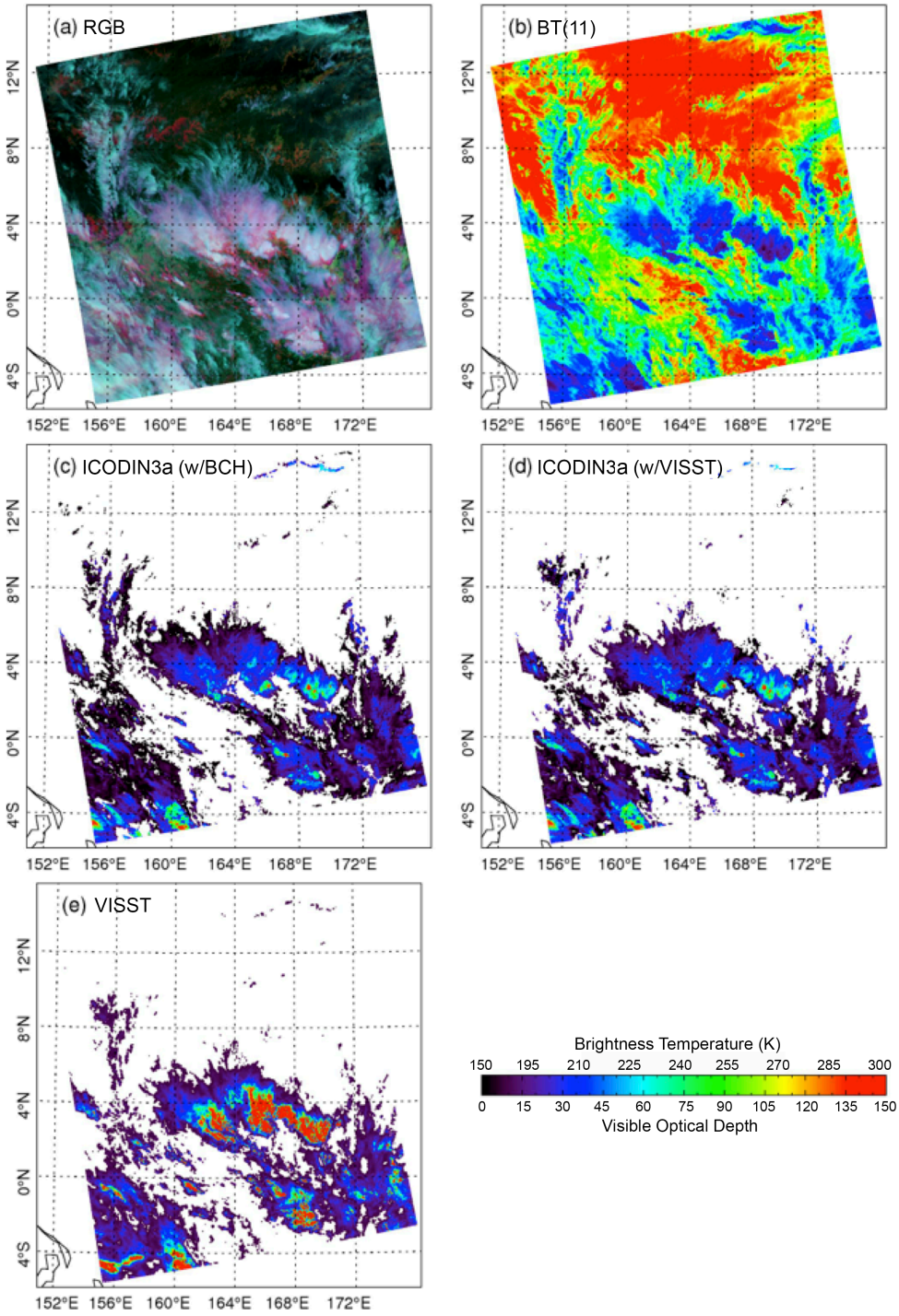

130

131 Figure 15. Comparison of cloud optical thicknesses estimated over western Pacific from daytime
132 Aqua MODIS data taken at 0235 UTC, 1 February 2007. (a) RGB [Red: 0.64 μm reflectance,
133 Green: BTD(3.7-11), Blue: BT(11)] image; (b) BT(11); τ_{CN3a} from ICODIN3a using (c) BCH
134 and (d) VISST to select opaque ice clouds; and (e) total cloud τ estimated using VISST.
135

136

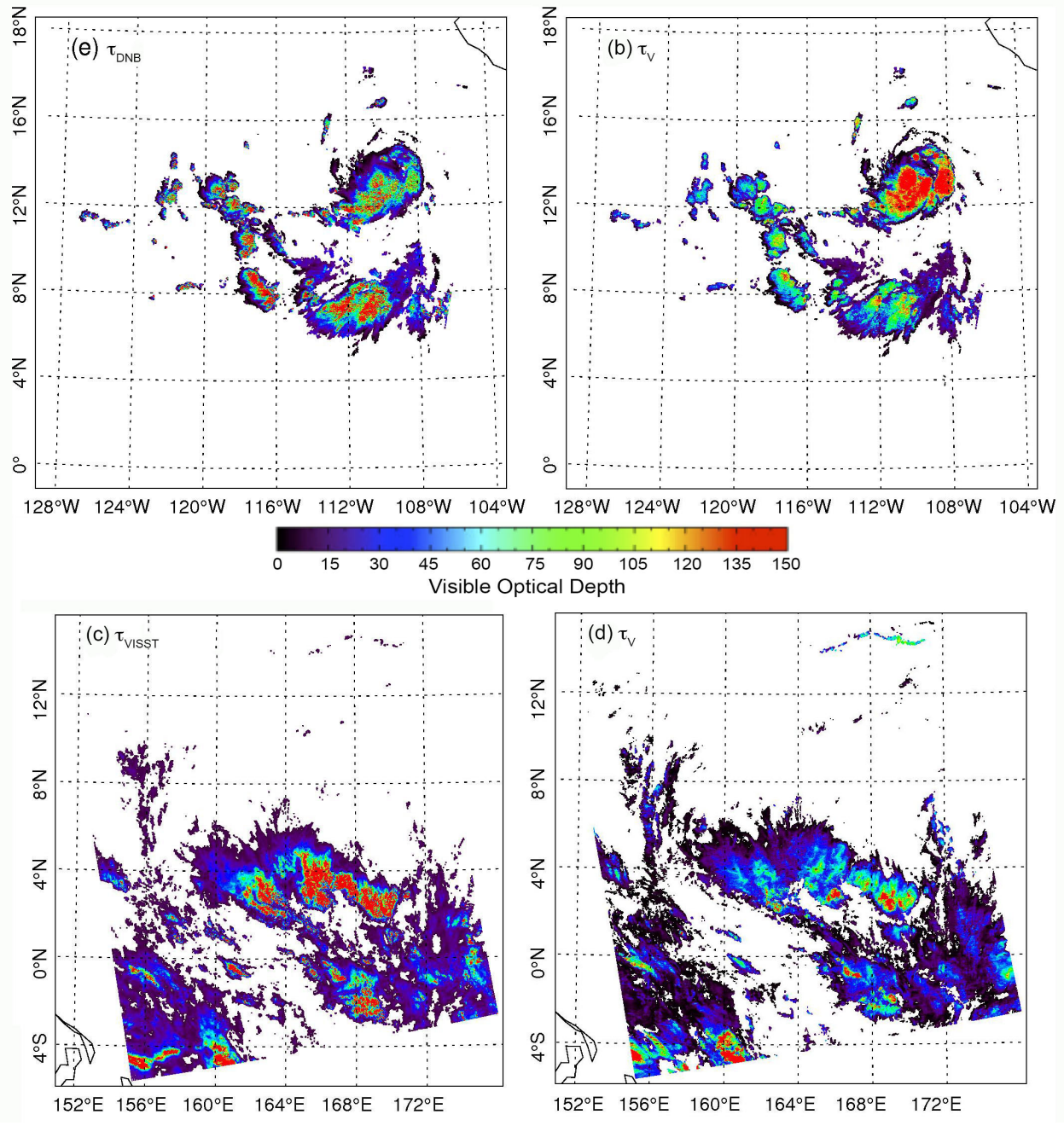

137

138 Figure 16. Cloud optical depths for images in (a & b) Figure 14a and (c & d) Figure 15a. Optical
139 depths derived from (a) VIIRS DNB channel, (b) τ_{CN4} and Eq (3), (c) MODIS visible channel,
140 and (d) τ_{CN3a} and Eq (3).

141

142